Comparing drag partition schemes over a herbaceous Sahelian rangeland

Caroline Pierre, G. Bergametti, B. Marticoréna, L. Kergoat, Éric Mougin, Pierre Hiernaux

To cite this version:

Caroline Pierre, G. Bergametti, B. Marticoréna, L. Kergoat, Éric Mougin, et al.. Comparing drag partition schemes over a herbaceous Sahelian rangeland. Journal of Geophysical Research: Earth Surface, 2014, 119 (10), pp.2291-2313. 10.1002/2014JF003177 . hal-02323513

HAL Id: hal-02323513

https://hal.science/hal-02323513

Submitted on 21 Oct 2019

HAL is a multi-disciplinary open access archive for the deposit and dissemination of scientific research documents, whether they are published or not. The documents may come from teaching and research institutions in France or abroad, or from public or private research centers.

L'archive ouverte pluridisciplinaire **HAL**, est destinée au dépôt et à la diffusion de documents scientifiques de niveau recherche, publiés ou non, émanant des établissements d'enseignement et de recherche français ou étrangers, des laboratoires publics ou privés.

AGU PUBLICATIONS

JGR

Journal of Geophysical Research: Earth Surface

RESEARCH ARTICLE

10.1002/2014JF003177

Key Points:

- Drag partition schemes are compared for a typical Sahelian herbaceous rangeland
- Seasonality of the shear velocity ratio is driven by the grass patch dynamics
- Simulated dust emissions are similar regardless of the drag partition scheme

Correspondence to:
C. Pierre,
caroline.pierre@get.obs-mip.fr

Citation:
Pierre, C., G. Bergametti, B. Marticorena, L. Kergoat, E. Mougin, and P. Hiernaux (2014), Comparing drag partition schemes over a herbaceous Sahelian rangeland, *J. Geophys. Res. Earth Surf.*, *119*, 2291–2313, doi:10.1002/2014JF003177.

Received 14 APR 2014
Accepted 30 SEP 2014
Accepted article online 3 OCT 2014
Published online 29 OCT 2014

Comparing drag partition schemes over a herbaceous Sahelian rangeland

C. Pierre[1], G. Bergametti[2], B. Marticorena[2], L. Kergoat[1], E. Mougin[1], and P. Hiernaux[1]

[1]Geosciences Environnement Toulouse (UPS/CNRS/IRD/CNES), Toulouse, France, [2]Laboratoire Interuniversitaire des Systèmes Atmosphériques, Université Paris Est Créteil and Université Paris Diderot, Institut Pierre Simon Laplace, Créteil, France

Abstract Modeling of dust emissions from the surface remains complex, especially in semiarid regions where vegetation must be accounted for because of its potentially important protective effect. Protection is directly linked to the fraction of the soil surface covered by vegetation, but it is also driven by the interaction of vegetation elements with the wind field. The sensitivity of simulated dust emissions to various drag partition schemes—mainly those proposed by Raupach (1992), Marticorena and Bergametti (1995), and Okin (2008)—is evaluated for a typical Sahelian rangeland, covered by a seasonal grass layer, over a complete vegetation cycle. The application of these schemes requires a fine characterization of the vegetation cover; field measurements from an ecological survey are used to derive the geometric dimensions of the grass patches. Models are run with meteorological forcing from automatic weather stations. As a result, the impacts of soil moisture and grass cover are estimated over April to September. Soil moisture inhibits dust emissions by 27% in mass. The different drag partition schemes exhibit distinctive limitations, mostly due to the properties of the Sahelian grass cover, which is composed of large and low patches of short grass, with a strong seasonal dynamics. However, the drag partition schemes result in remarkably coherent estimations of dust emissions. When soil moisture is taken into account, vegetation reduces the total vertical mass fluxes by 6 to 26% of the emissions of a bare soil, depending on the drag partition scheme.

1. Introduction

Wind erosion displaces large amounts of sediment from the ground surface and leads to the injection of mineral dust into the atmosphere. At the local scale, in semiarid areas where soils support crop production and/or fodder production, wind erosion can be responsible for significant losses of surface soil [see, for example, *Michels*, 1994]. Additionally, the injection of large amounts of mineral dust into the atmosphere by soil erosion not only affects air quality and thus human health [e.g., *Ozer*, 2008; *de Longueville et al.*, 2013] but also raises difficulties in the management of infrastructure. For example, the reduction in horizontal visibility caused by high dust concentrations induces disruptions of air and road traffic in the vicinity of the source regions [e.g., *Pauley et al.*, 1996].

At the global scale, dust emitted from arid and semiarid areas represents more than 30% of the total amount of aerosols injected into the atmosphere each year [*Boucher et al.*, 2013]. When deposited in continental and oceanic regions, mineral particles can play a decisive role in the availability of nutrients such as iron or phosphorus [e.g., *Swap et al.*, 1992; *Jickells et al.*, 2005]. Mineral dust also affects the radiative balance of the Earth and thus its climate: because mineral dust contributes on average up to 20% of the total aerosol optical thickness across the globe, it significantly backscatters and/or absorbs solar and telluric radiation. Moreover, Saharan mineral dust particles have shown to be effective ice nuclei [*Rosenfeld et al.*, 2001; *Sassen et al.*, 2003] that are able to modulate climate through cloud interactions.

In the forthcoming decades, a significant change in the dust content of the atmosphere is expected, mainly caused by a changing contribution to dust emissions by semiarid areas [*Boucher et al.*, 2013]. Studies in the last three decades have reported significant progress in terms of modeling the processes involved in dust emission, mostly based on explicit physical parameterizations [*Gillette and Passi*, 1988; *Raupach*, 1992; *Marticorena and Bergametti*, 1995; *Shao et al.*, 1996; *Li et al.*, 2013, among others]. Because of these improvements, the factors controlling dust emission and their hierarchy are now better understood [e.g., *Marticorena et al.*, 1997; *Darmenova et al.*, 2009].

However, it remains difficult to distinguish the contribution of bioclimatic changes and anthropogenic pressure in terms of the evolution of the global dust emissions. Indeed, estimations of the anthropogenic

©2014. American Geophysical Union. All Rights Reserved.

contribution to the atmospheric dust load are variable. *Tegen and Fung* [1995] estimated that 30 to 50% of the total atmospheric dust load is due to climatic changes and human activities. Several years later, *Tegen et al.* [2004] estimated a contribution from “land use sources” of 10%, in comparison to an estimate of 0 to 50% reported by *Mahowald et al.* [2004], who used the same data but a different model and methodology. A recent study by *Yoshioka et al.* [2005] based on comparisons between simulations and observations (the Absorbing Aerosol Indices derived from Total Ozone Mapping Spectrometer measurements) yielded a contribution of 0 to 25% from new desert (i.e., dry and unvegetated areas in 1980–1984 but not in 1965–1969) and cultivation sources. Considering the Sahel more specifically, *Cowie et al.* [2013] observed a decrease in Sahelian dust emissions since approximately 1980, which could be due to both an increase in the surface roughness induced by vegetation and a decrease in wind speed. The simulations of dust emissions from the Sahelian belt by *Pierre et al.* [2012] suggested that an undisturbed Sahel (i.e., without accounting for land use such as cultivation and pasture) should not be a major dust source.

However, the simulations of *Pierre et al.* [2012] did not address the limitations linked to the effects of the vegetation structure on the distribution of the wind energy transferred on the surface. Indeed, the roughness density, which is the density of obstacle frontal areas, is widely used by existing models. Vegetation is usually treated as individual obstacles, such as bushes or grass tussocks, and its seasonal dynamics are not often considered. Additionally, most studies dealing with dust emissions in vegetated areas consider nonerodible elements (pebble, stones, and vegetation) to be homogeneously distributed. Recently, several studies have focused on these issues concerning woody obstacles. The impact of the size and spatial distribution of trees and bushes has been studied by *Dupont et al.* [2014] using numerical simulations, highlighting the significant impact of obstacle orientation with respect to the main wind direction. Similarly, based on wind tunnel measurements on artificial shrubs, *Youssef et al.* [2012] concluded that the aeolian flux within a land unit is affected by the neighboring land units and by the vegetation pattern within both the unit itself and the neighboring land units. The distribution pattern of woody plants can be critical, particularly if they form “streets” where wind erosion is enhanced, as observed by *Okin and Gillette* [2001] or *Bergametti and Gillette* [2010] for mesquites in the Chihuahuan Desert. Likewise, using the wind tunnel measurements on solid obstacles in various configurations reported by *Brown et al.* [2008], *Webb et al.* [2014] noted the inability of the current drag partitioning approaches to reproduce its sensitivity to roughness configuration. This sensitivity is caused by the spatial variability of the shear stress, particularly when its distribution is close to the threshold for soil entrainment. According to *Webb et al.* [2014], this limitation yields strong overestimates of aeolian sediment fluxes by the models.

In Sahelian ecosystems, trees and bushes are generally scattered over deep sandy soils, while they can form thickets on shallow and fine-textured soils. The structure of the woody population changes very little over short time scales (seasons to several years). The herbaceous layer is a major obstacle to wind in the Sahel and in many grasslands worldwide [e.g., *Ludwig and Tongway*, 1995; *Armas et al.*, 2008; *Wang et al.*, 2008]. It can be highly discontinuous depending on the season, soil texture, and small-scale topography, being clumped into patches that are more or less disconnected. Thus, for this type of surface, the rainfall dynamics make use of a static representation of the surface properties in the models problematic. Additionally, the herbaceous pattern in rangelands differs markedly from that of crops due to its specific geometry and organization. Regarding perennial grass, *Chepil and Woodruff* [1963] even stated that it “affords one of the best protective covers because it is finer than most cultivated crops, has a relatively great protective surface both above and below the surface of the ground, and is well anchored.” Therefore, grass cover might be considered efficient in controlling wind erosion to preserve the yields in croplands [*Lyles and Allison*, 1980; *Fryrear and Skidmore*, 1985] or the grazing resources in rangelands [*Li et al.*, 2005]. Thus, there is a need to better characterize the uncertainties in dust modeling over such vegetated surfaces by paying specific attention to the herbaceous layer and its dynamics.

The objective of the present study is to estimate the impact of the use of different drag partition schemes on dust emission simulations in the case of a typical Sahelian rangeland, which is covered by a seasonal herbaceous layer. For that purpose, a fine-scale representation of this grass cover and of its seasonal dynamics is proposed, based on a specific methodology and field measurements. The parameters required for the application of the drag partition schemes are derived from these measurements and from the literature (section 2). The dust emissions simulated by using these different drag partition schemes are compared over a seasonal cycle (section 3) before concluding (section 4).

©2014. American Geophysical Union. All Rights Reserved.

2. Materials and Methods

2.1. Field Site and Data

2.1.1. Field Site Description

The Gourma region in Mali is representative of the semiarid, noncultivated Sahel. It is located within the Sahelian bioclimatic zone, with annual rainfall ranging between 100 and 600 mm. It harbors a long-term ecosystem monitoring program (since 1984) [*Mougin et al*., 2009], which is particularly focused on vegetation observations obtained along twenty-five 1 km lines (or transects) distributed along a north-south bioclimatic gradient, within the frame of the African Monsoon Multidisciplinary Analyses–Couplage de l'Atmosphère Tropical et du Cycle Hydrologique (AMMA-CATCH) observatory [e.g., *Hiernaux et al*., 2009]. Sites were selected to account for different soil types (sandy, loamy clay, and shallow soils), and three different levels of grazing pressure (low, moderate, and intense) were investigated for the dominant sandy soils. Among them, the sandy site at Agoufou (15.34°N, 1.48°E) was measured most frequently. The year 2007 is chosen here for vegetation measurements because of its high sampling rate (10 measurement dates ranging from the beginning of April to the end of September), allowing a fine representation of the vegetation seasonality which is well marked in the Sahel.

2.1.2. Data Sets

2.1.2.1. Vegetation Data

The survey of the 1 km lines was primarily aimed at estimating the herbaceous mass at this scale, but it provided data that can be used to characterize the parameters required by drag partitioning schemes. At each visit, every 1 m × 1 m plot along the 1 km line was visually classified into four classes: bare soil and low, medium, and high herbaceous mass. Then, the average mass of each class was estimated through six destructive samples for the medium class and three for the low and high classes. For these samples, all the vegetation was cut, dried, and weighed. Litter and standing stems were collected separately. This protocol has been shown to be efficient in providing data for many sites over the long term [*Hiernaux et al*., 2009].

2.1.2.2. Derivation of the Grass Patch Characteristics

Drag partition schemes require different inputs, such as the geometry of the vegetation obstacles, their roughness density (ratio of the sum of the obstacles' frontal areas, face to wind, per unit soil area), and the erodible surface fraction (see section 2.2). To derive these parameters, the grass layer is represented as a collection of grass patches (of width W, height H, and length L), whose size varies with the season. The length of the patches and the interpatch distance are derived from the 1 km line classification and mass data, and the roughness density (λ) is in turn derived from the size and density of the patches and the grass height. Similar to *Okin* [2005] and assuming square-shaped grass patches ($W = L$), λ can be expressed as a function of the dimensions of the grass patches:

$$\lambda = \frac{nWH}{S} = \frac{nW^2}{S}\frac{H}{W} = F_{cv}\frac{H}{W} \tag{1}$$

where n is the number of grass patches for a given surface S and F_{cv} is the cover ratio of the surface by vegetation.

The mean grass height H is estimated from the herbaceous mass M using an empirical equation derived for the Agoufou site [*Mougin et al*., 1995, updated equation (28)]:

$$H = -2.4\ 10^{-7}M^2 + 5.5\ 10^{-4}M + 4.7\ 10^{-2} \tag{2}$$

with H in meter and M in kg ha^{-1}.

Along each 1 km line, patches are defined as sequences of plots whose standing mass is larger than a fixed threshold. Below this threshold, there are risks of soil erosion; above it, the soil is considered to be protected from erosion. In line with the literature (see Appendix A), a lower bound of 10 g m^{-2} is retained, and plots with more than 10 g m^{-2} standing mass are considered to be nonerodible obstacles. Because the 1 km classification raw data are aggregated during the field survey in groups of 10 consecutive 1 m × 1 m plots, for each date, an ensemble series of 1 m × 1 m masses are obtained with a random disaggregation scheme (Appendix A). The average length of the grass patches W is computed over the ensemble of randomly disaggregated series. The density of the patches is derived from the patch length and the obstacle cover ratio

©2014. American Geophysical Union. All Rights Reserved.

along the 1 km line, F_{cv}, which is computed as the fraction of plots above 10 g m^{-2}. An interpatch distance D can then be derived:

$$F_{cv} = \frac{W^2}{(W+D)^2} \quad \text{thus} \quad D = W\,\frac{1-\sqrt{F_{cv}}}{\sqrt{F_{cv}}} \tag{3}$$

The mass threshold for defining a grass patch is applied to standing mass only (green vegetation + straws) and does not consider litter. However, litter has a protective effect on the surface [e.g., *Li et al.*, 2005]. The fraction of erodible surface (E) is then computed considering plots with a sum of litter, straw, and green vegetation below the threshold of 10 g m^{-2}.

2.1.2.3. Soil and Meteorological Data

At the Agoufou site, the soil is sandy, and the proportion of clay ($\%_{\text{clay}}$) ranges from 0.5 to 1% [*De Rosnay et al.*, 2009] (Table 7). Soil moisture was measured at 5 cm depth every 15 min with CS116 probes (Campbell Scientific). The shallow soil moisture (at 1 cm depth) was derived from the 5 cm depth measured values by assuming a linear moisture decrease with time yielding to no soil moisture after 36 h without rain, in agreement with the time required for the albedo to retrieve its normal value after a rain event [*Samain et al.*, 2008]. Fifteen minutes of cumulated rainfall was recorded at the same location. The wind speed was monitored at 4.2 m elevation every 5 min with a CSAT3 anemometer.

In the Sahel, a significant part of dust emission events are driven by gusts associated with the cold pool outflows of convective systems. These gusts can be followed by convective rainfall with a typical time lag on the order of 30 min. This lag varies considerably, and in some cases, no rain follows the gust at all. Given the strong inhibiting effect of soil moisture on dust emission [e.g., *Fécan et al.*, 1999] and the importance of the short-term variations in wind and rainfall, consistency between wind and soil moisture data is important. Because wind data are missing during April 2007 for the Agoufou site, a consistent set of meteorological data from 2008 (wind and soil moisture) is used. As vegetation measurements are provided at 10 dates over a 6 month period in 2007, the characteristics of the herbaceous cover derived from these measurements are also assumed to be representative of the 2008 seasonal vegetation cycle.

2.2. Drag Partition Schemes

The wind provides energy to the surface, which is applied as a shear stress τ on the surface and the obstacles [*Raupach*, 1992] defined as follows:

$$\tau = \rho\, {u_*}^2 \tag{4}$$

where ρ is the air density and u_* is the wind friction velocity.

This energy provided by the wind is divided over nonerodible elements, such as pebbles and vegetation, and the intervening surface according to the drag partition. Several drag partition schemes have been derived from different conceptual bases. The schemes compared in this study are representative of these approaches. Two of the schemes require as input data either the ratio of the obstacle to the surface drag coefficients (β) and the roughness density (λ) [*Raupach et al.*, 1993] (section 2.2.1) or the aerodynamic roughness length of the surface Z_0 [*Marticorena and Bergametti*, 1995] (section 2.2.2). These schemes are particularly relevant for relatively low roughness density and uniformly distributed obstacles [*Shao and Yang*, 2005; *Darmenova et al.*, 2009]. An alternative model, specifically designed for heterogeneously vegetated surfaces, has been proposed by *Okin* [2008] (section 2.2.3). The last model is a formulation of the shear stress over a discontinuous vegetation cover that has been developed in the framework of this study. It is based on parameterizations from *Raupach* [1992] and on a wind flow model originally designed for applications in urban areas and later applied to vegetation canopies (section 2.2.4).

2.2.1. Scheme Based on the Drag Coefficient

A theoretical approach and analytic development (using dimensional analysis) were proposed by *Raupach* [1992] based on two hypotheses: (i) the existence of a sheltered area and a sheltered volume downwind of each obstacle and (ii) the random superimposition of these sheltered areas and volumes when the obstacles are close to each other. This drag partition scheme determines the ratio between the average shear stress on the soil surface τ_s (or on the exposed soil surface, τ_s') and the shear stress τ exerted over the entire surface (including obstacles) based on the estimation of the force exerted on the obstacles.

©2014. American Geophysical Union. All Rights Reserved.

Because the shear stress around obstacles can exhibit spatial heterogeneity, *Raupach et al*. [1993] introduced an additional parameter (ranging between 0 and 1), called *m*, to represent this phenomenon. More precisely, the *m* parameter multiplies the roughness density λ to estimate the maximum shear stress $\tau_s{}'$ as opposed to the average shear stress $\tau_s{}'$. The expression of the drag partition thus becomes

$$\frac{u_{s*}}{u*} = \sqrt{\frac{\tau''_s}{\tau}} = \frac{1}{\sqrt{(1 - m\sigma\lambda)(1 + m\beta\lambda)}} \tag{5}$$

where u_{S*} and u_* are the friction velocity exerted on the surface between obstacles and the total friction velocity, respectively. The parameters m, σ, and β refer to the differences between the average substrate surface stress and the maximum stress on the surface at any one point, the basal to frontal area ratio of the obstacle, and the ratio of an isolated obstacle to the bare surface drag coefficients, respectively.

By fitting the required parameters in Raupach's parameterization, a good agreement has been obtained between this drag partition scheme and wind tunnel measurements [*Marshall*, 1971; *Musick et al*., 1996; *Crawley and Nickling*, 2003; *Brown et al*., 2008]. Based on field measurements for sparsely vegetated sites (typically $\lambda < 0.2$), *Wolfe and Nickling* [1996], *Wyatt and Nickling* [1997], and *Lancaster and Baas* [1998] have established the validity of this model when all the dimensions of the obstacles are known. However, the determination of the drag coefficient for the obstacles, the surface, and the *m* parameter is challenging, especially for regional modeling purposes.

2.2.2. Scheme Based on the Aerodynamic Roughness Length

A spatially integrative approach to the drag partition, focusing on the wind profile properties, has been proposed by *Marticorena and Bergametti* [1995], following *Arya* [1975]. The authors assume that for low roughness density ($\lambda = nWH/S < 0.05$, with n as the number of obstacles for a given ground surface S and W and H as their width and height, respectively), an internal boundary layer (IBL) develops behind each obstacle. It is further assumed that both this IBL and the atmospheric boundary layer (ABL) above the obstacles can be characterized by logarithmic wind profiles in neutral conditions, driven by their respective aerodynamic roughness Z_0. Using the expressions of the two wind profiles (IBL and ABL), *Marticorena and Bergametti* [1995] defined an efficient fraction f_{eff} as the ratio of the wind friction velocity over the bare erodible surface (between obstacles) and the wind friction velocity for the whole surface including the effects of obstacles on the wind profile in the ABL:

$$\frac{u_{s*}}{u*} = f_{\text{eff}} = 1 - \frac{\ln\left(\frac{Z_0}{z_{0s}}\right)}{\ln\left(\left(0.7 * \left(\frac{X}{z_{0s}}\right)\right)^{0.8}\right)} \tag{6}$$

where z_{0s} is the aerodynamic roughness of the bare soil, Z_0 is the aerodynamic roughness of the surface (including the obstacles), and X is the mean distance downstream from the point of the roughness discontinuity, where the height of the IBL is computed (z_{0s}, Z_0, and X are in centimeter). In the original scheme, mainly targeted to compute dust emissions from arid deserts without vegetation, X was taken as 10 cm.

This parameterization of the drag partition has been tested against wind tunnel measurements at low roughness density for homogeneously distributed obstacles [from *Marshall*, 1971], and it was shown that it simulates the measured drag with the same confidence level and generated similar errors at high roughness densities as the Raupach's scheme [*Marticorena and Bergametti*, 1995]. This scheme was also used to reproduce the threshold wind friction velocities measured in situ using a wind tunnel over a variety of nonvegetated surfaces [*Marticorena et al*., 1997].

To account for typical desert vegetation effects, *MacKinnon et al*., 2004 adjusted the Marticorena and Bergametti's drag partition scheme to in situ measurements (Central Mojave Desert, USA); this adjustment mainly concerns the fitting of the distance downstream from the obstacle at which the height of the IBL should be computed. Obviously, for higher and larger obstacles such as vegetation, this change leads to a significant increase in the X value (in this case equal to 12,255 cm).

The applicability domain of this drag partition scheme is limited to surfaces with low roughness density ($\lambda<0.05$) [*Arya*, 1975; *Marticorena and Bergametti*, 1995], i.e., situations where the obstacles are distant enough for an IBL to develop. Additionally, the obstacles must be homogeneously distributed so that the Z_0

©2014. American Geophysical Union. All Rights Reserved.

parameter is relevant to assess the drag partition over the rough surface being considered. According to *King et al*. [2005], the Marticorena and Bergametti's model agrees well with laboratory measurements, while the Raupach's model agrees well with both laboratory and field measurements. However, *King et al*. [2005] did not test Mc Kinnon's adaptation.

2.2.3. Scheme for Heterogeneously Vegetated Surfaces

In semiarid rangelands, the structure of the vegetation may play a predominant role in the drag partition, as shown for a mesquite-dominated area in the Chihuahuan Desert [*Okin and Gillette*, 2001; *Bowker et al*., 2008; *Bergametti and Gillette*, 2010]. As mentioned by *Darmenova et al*. [2009], who considered the Marticorena and Bergametti's model, "The drag partition correction in this approach has two intrinsic limitations: (1) it is valid for small wakes ($Z_0 < 1$ cm) and (2) it was developed to parameterize solid obstacles only. This poses a problem in applying this approach to partially vegetated surfaces such as mixed rangelands, shrublands, and agricultural/shrubland mosaics." Similarly, *Shao and Yang* [2005] presented a theoretical argument that the Raupach's scheme was limited to $\lambda < 0.1$.

An approach describing the spatial distribution of shear stress in a vegetated area is a relevant alternative to assess the drag partition of a vegetated surface. Particularly, it can represent dust emission even at high roughness densities, keeping in mind that the same roughness density can be obtained for obstacles with different dimensions. Addressing this issue, *Okin* [2008] proposed a model based on a probabilistic function to dimension the unvegetated gaps between plants to assess the friction velocity in the lee of the plants. In this scheme, the spatial evolution of the friction velocity is based on the measurements of friction velocities downwind of a porous fence [*Bradley and Mulhearn*, 1983], which are scaled by Okin to asymptotically reach, far from the fence, the value corresponding to the friction velocity upwind of the fence. This model requires the vegetation height, the average gap size between the plants, and the shear velocity ratio right behind the obstacle (that can be obtained by adjustment to measurements). The Okin's scheme has been compared to the Raupach's and Marticorena and Bergametti's drag partition by *Li et al*. [2013]. The authors show that on vegetated surfaces, the latter models do not predict any horizontal flux when a sediment flux is actually measured in the field, whereas Okin's model does. To explain this different behavior of the various drag partition schemes, the authors underline the importance of accounting for the vegetation distribution and the local variability of the shear stress on the surface around the plants.

By integrating equation (4) in *Okin* [2008] and considering a gamma distribution for the gap sizes following this author (equation (3) in *Okin* [2008]), the drag partition can be expressed in an integrative way:

$$\frac{u_{s*}}{u*} = \frac{L + cU_0}{L + c} \tag{7}$$

where L is the mean interobstacle distance, c is a characteristic length of the wake, and U_0 is the u_{S*}/u_* value right behind an obstacle. However, note that equation (7) indicates an integrated value of the energy transmitted to the surface between obstacles, while Okin's scheme probabilistically represents u_{S*} variations in the lee of each obstacle and therefore emissions that are not simply related to this ratio.

2.2.4. A Drag Partition Scheme Combining a Wind Field Model and Raupach's Parameterization

According to *Raupach* [1992, equation (11), p. 382], the equivalent area A for which the surface shear stress τ is zero relates to the width (W) and height (H) of an obstacle as follows:

$$\frac{\tau_s(\lambda)}{\tau(\lambda = 0)} = e^{-\lambda A/_{WH}} \tag{8}$$

If two successive grass patches are distant, erosion processes can be considered distinctly: (1) for the bare surface between the two vegetation patches, (2) inside a given vegetation patch, and (3) in the transitional zone around the vegetation patch, where the airflow is disturbed by the proximity of the obstacle. Following the approach of *Okin* [2008], a new scheme is proposed that considers the description of the shear stress between the herbaceous patches. This scheme aims to estimate the area A from the geometrical properties of the obstacles. It is built by (i) using a semiempirical mass-consistent diagnostic wind field model, QUIC (Quick Urban and Industrial Complex), to describe the cavities downwind and upwind of the obstacles, and (ii) using parameterizations developed by *Raupach* [1992] to assess the increase in the total shear stress with increasing roughness density. The description of the shear stress exerted on the surface in the cavities is

Table 1. Values of the Constant Parameters for the Selected Drag Partition Schemes to be Compared

Drag Partition Scheme	Parameter Values	Reference
RW $\frac{u_S{}^*}{u^*} = \frac{1}{\sqrt{(1-m\sigma\lambda)(1+m\beta\lambda)}}$	$m = 0.71$, $\sigma = 0.125$, and $\beta = 93$	*Walter et al.* [2012]
RW17 same as RW	σ from field measurements	*Walter et al.* [2012] for m and β
MB $\frac{u_S{}^*}{u^*} = 1 - \frac{\ln\left(\frac{Z_0}{z_{0s}}\right)}{\ln\left(\left(0.7^*\left(\frac{12\ 255}{z_{0s}}\right)\right)^{0.8}\right)}$	$z_{0s} = 0.0097$ cm	*Abdourhamane Touré et al.* [2011] and *Pierre et al.* [2014]
OK $\frac{u_S{}^*}{u^*} = \frac{L+cU_0}{L+c}$	$c = 5.7$	*Li et al.* [2013]
	$U_0 = 0.31$	
RQ $\frac{u_S{}^*}{u^*} = \sqrt{e^{-\lambda A/_{WH}}\ C_s\ \left(\frac{U_h\ (\lambda)}{U^*\ (\lambda)}\right)^2\ \frac{1}{F_{bare}}}$	$c = 1$	*Raupach* [1992]
	$C_S = 0.0017$ and $C_R = 0.166$	*Walter et al.* [2012]
RQskim same as RQ	$u_{S*}/u_* = 0.31$ with interfering perturbations	*Li et al.* [2013]

derived from the literature. Details of the computations can be found in Appendix B. These two steps yield a new formula for the equivalent area A, where the shear stress is nil. Finally, the drag partition is expressed by

$$\frac{u_{s*}}{u*} = \sqrt{\frac{\tau'_s}{\tau}} = \sqrt{e^{-\lambda A/_{WH}}\ C_s\ \left(\frac{U_H\ (\lambda)}{U^*\ (\lambda)}\right)^2\ \frac{1}{F_{\text{bare}}}} \qquad (9)$$

where F_{bare} is the fraction of bare surface, C_S is the drag coefficient of the bare soil, and $\left(\frac{u_H\ (\lambda)}{u*\ (\lambda)}\right)$ can be computed iteratively following *Raupach* [1992].

2.3. Parameters for the Drag Partition Scheme

Drag partition schemes require a set of parameters to be prescribed. When possible, these values are obtained from the literature dealing with obstacles as similar as possible to the herbaceous vegetation considered here (Table 1).

Several studies have aimed to estimate the parameters of Raupach's scheme for vegetated surfaces, such as *Gillies et al.* [2002] for three plant species from wind tunnel experiments, *King et al.* [2005] for the β and m parameters for a set of various wind tunnel and field experiments, or *King et al.* [2006] for the m parameter in the case of mesquites in New Mexico. The recent study by *Walter et al.* [2012], which proposes values for these parameters based on measurements performed with live grass tussocks, is the most relevant to represent specifically herbaceous vegetation. The scheme using these parameters is referred to as RW for "*Raupach–Walter*." An alternative formulation of the same scheme is tested (RW17, the number 17 referring to the Agoufou site's number in past literature) by deriving the σ parameter (also called the aspect ratio: the ratio of the basal to frontal areas of the obstacle—thus $= W/H$ for square-shaped grass patches) from the dimensions of the obstacles at the Agoufou site, while the parameters m and β keep the values defined by *Walter et al.* [2012]. The version of the Marticorena and Bergametti's scheme (MB) used here is the one adapted by *MacKinnon et al.*, 2004. The aerodynamic roughness length of the bare soil (z_{0s}) is derived from a previous study over a similar sandy soil [*Abdourhamane Touré et al.*, 2011; *Pierre et al.*, 2014], and the aerodynamic roughness length of the entire surface (Z_0) is obtained from the empirical parameterization of *Marticorena et al.* [2006] established for rangelands in Tunisia:

$$\ln(Z_0/H) = \begin{cases} 1.31\ ln(\lambda) + 0.66 & if \quad \lambda < 0.045 \\ -1.16 & \qquad \text{otherwise.} \end{cases} \qquad (10)$$

The input parameters of the Okin's scheme (OK) are selected from *Li et al.* [2013, Table 6] by using the values associated with the *Kawamura*'s [1951] parameterization of the horizontal flux, which is used here (see section 2.4). Finally, the required parameters of the drag partition scheme combining Raupach's and the QUIC model (RQ) are taken from *Raupach* [1992] and *Walter et al.* [2012], while an alternative formulation (RQskim) is proposed to take into account the interference between the perturbations of airflow (cases of "skimming flow"), for which the ratio u_{S*}/u_* is considered to be constant when the sum of the upwind frontal eddy and downwind reversed cavity is larger than the distance between the obstacles. Because the RW17 and RQ schemes imply a division by the proportion of the surface not covered by obstacles (i.e., standing herbaceous vegetation, dry, and green), which can be very low (because $1 - m\sigma\lambda \sim 1 - \sigma\lambda$ in equation (2) and F_{bare} in equation (7)), they are bounded to 1.

©2014. American Geophysical Union. All Rights Reserved.

Table 2. Simulation Setups for Dust Emissions[a]

	No Soil Moisture	Soil Moisture Derived From Measurements
Bare surface	Bare and Dry	Bare and Wet
Erodible surface fraction	E and Dry	E and Wet
Erodible surface fraction and drag partition	Vegetated and Dry	Vegetated and Wet

[a] The two Bare cases use a friction velocity for a bare surface ($u_{*\mathrm{bare}}$), while the other four cases use a friction velocity for a vegetated surface ($u_{*\mathrm{vgt}}$).

2.4. Calculation of Dust Emissions

Aeolian transport occurs only when the force exerted by the shear stress exceeds those maintaining the soil grains at the surface. The threshold wind friction velocity depends on the presence of nonerodible elements on the surface [*Bagnold*, 1941; *Gillette*, 1979], as expressed by the drag partition scheme, and on the topsoil layer characteristics (e.g., surface soil moisture, crusting, and grain size distribution). Indeed, the presence of water strengthens the cohesive forces linking the soil grains together and thus increases the threshold wind friction velocity. This effect can be computed using the empirical relationship proposed by *Fécan et al.* [1999]:

$$u_{*tw} = \begin{cases} u_{*t} & \text{if } w < w_0 \\ u_{*t}\left[1 + 1.21(w - w_0)^{0.68}\right]^{0.5} & \text{if } w > w_0 \end{cases} \tag{11}$$

where u_{*tw} is the threshold friction velocity for wet soil and u_{*t} for bare soil, w is the gravimetric soil moisture, and w_0 is the residual gravimetric soil moisture (in % g g^{-1}), which depends on the soil texture. The residual soil moisture w_0 is derived from the soil clay content following *Fécan et al.* [1999] as follows: $w_0 = 0.0014\,(\%_{\mathrm{clay}})^2 + 0.17\,(\%_{\mathrm{clay}})$. This yields a residual soil moisture close to zero for the Agoufou site.

The friction velocity is computed from the wind speed and aerodynamic surface roughness (Z_0) assuming a logarithmic wind profile [*Priestley*, 1959]:

$$u_* = k\frac{U(z)}{\ln\left(\frac{z}{Z_0}\right)} \tag{12}$$

where k is the von Karman constant ($k = 0.4$)

Because wind measurements were collected on the vegetated Agoufou site, the friction velocity for a bare soil situation ($u_{*\mathrm{bare}}$) is estimated from these measurements by assuming a free stream wind velocity at an elevation of 50 m:

$$u_{*\mathrm{bare}} = u_{*\mathrm{vgt}}\,\frac{\ln\left(\frac{50\ \mathrm{m}}{Z_0}\right)}{\ln\left(\frac{50\ \mathrm{m}}{z_{0s}}\right)} \tag{13}$$

where $u_{*\mathrm{vgt}}$ is the friction velocity deduced from equation (12).

When the threshold friction velocity is exceeded, particle entrainment occurs, and the particle mass flux depends on a power function of the wind friction velocity. The horizontal flux G (in kg m^{-1} d^{-1}) is estimated following *Kawamura* [1951] and *White* [1979], taking into account (in some cases, see below) the fraction of erodible surface E. The vertical flux F (kg m^{-2} d^{-1}), composed of particles with diameters smaller than approximately 20 μm [*Laurent et al.*, 2006], is estimated from the horizontal flux G following *Marticorena and Bergametti* [1995], who derived the content of fine particles from the soil clay content. Accordingly, the ratio between the fluxes has been taken as $^F/_G = 1.12 \times 10^{-6}$ m^{-1}, as for the Agoufou sandy area in the data set used by *Pierre et al.* [2012].

The porosity [*Gillies et al.*, 2002; *Minvielle et al.*, 2003; *Shinoda et al.*, 2011] and the flexibility [*Gillies et al.*, 2002; *Ortiz et al.*, 2013] of the obstacles are not considered explicitly because no parameterization has been designed specifically for herbaceous patches and since these parameters can have various effects. For example, *Gillies et al.* [2002] highlighted the distinctive behavior of two bush species (burning bush and Colorado blue spruce) that exhibit a decreasing frontal area and increasing optical porosity with increasing wind speed, while the grass species (fountain grass) exhibit an ever decreasing drag coefficient for increasing wind speed, as well as decreasing frontal area and optical porosity. However, when possible, the values

©2014. American Geophysical Union. All Rights Reserved.

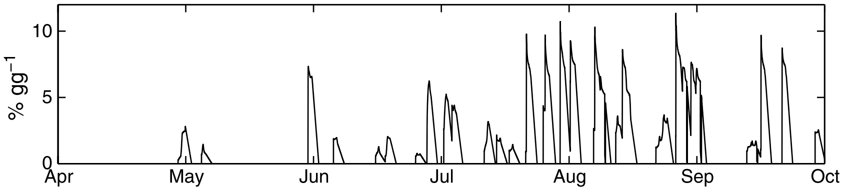

Figure 1. Gravimetric soil moisture at 1 cm estimated from measurements performed at 5 cm depth, Agoufou site, 2008.

resulting from measurements performed on herbaceous obstacles are used here (see Table 1) in order to take into account these properties. Several simulations have been designed to provide a bench mark for the drag partition schemes and to investigate the role of different factors, namely, soil moisture, erodible soil fraction, and drag partition. The simulation setups are summarized in Table 2.

The “Bare and Dry” case provides a reference value for a bare and dry surface, while the “Vegetated and Wet” case provides the simulated dust emissions in real conditions. The differences between the “E and Dry” and “E and Wet” cases, as well as between the “Vegetated and Dry” and Vegetated and Wet cases, document the role of soil moisture on dust emission simulations. The two “E” cases use a friction velocity for a vegetated surface without taking into account the drag partition. The differences between the E and Dry and Vegetated

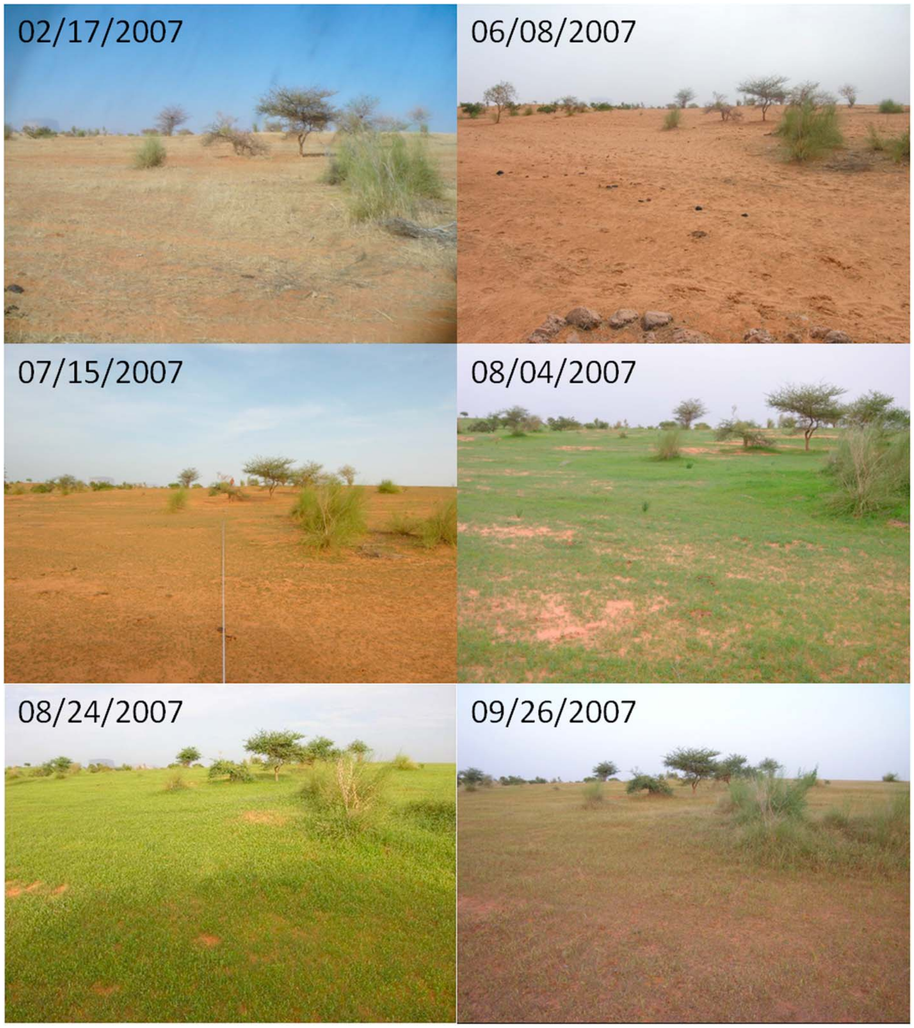

Figure 2. Rangeland in Gourma, Mali (Agoufou site, 15.34°N, 1.48°E), 2007. Pictures taken within the frame of the African Monsoon Multidisciplinary Analysis/Couplage de l’Atmosphère Tropical et du Cycle Hydrologique (AMMA-CATCH) Program.

©2014. American Geophysical Union. All Rights Reserved.

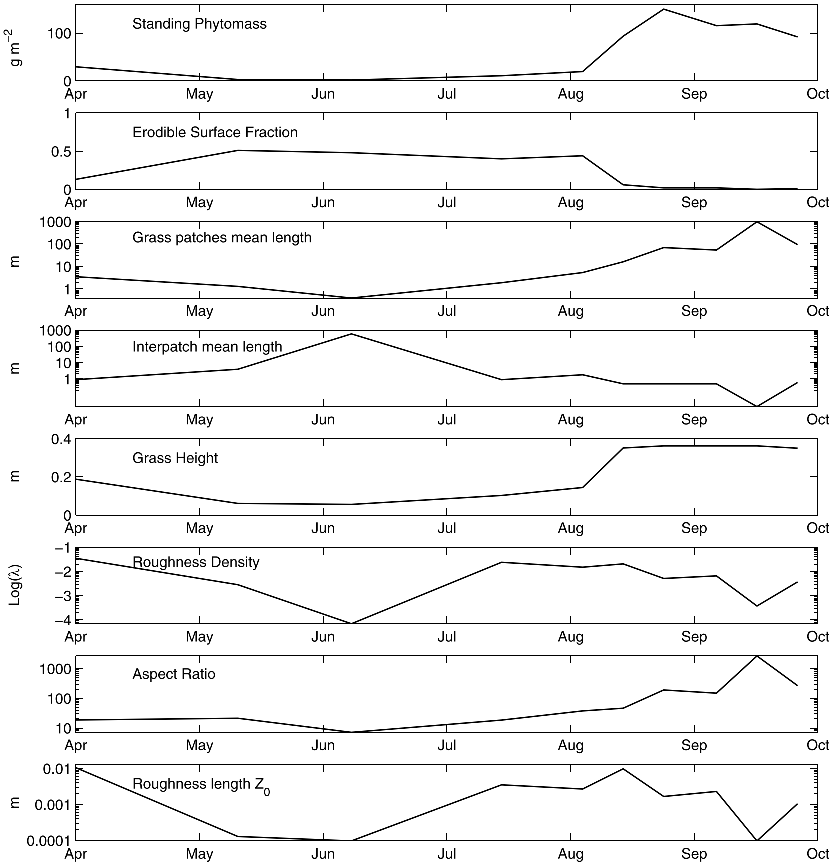

Figure 3. Characteristic values of the vegetation cover at the Agoufou site, 2007.

and Dry cases and between the E and Wet and Vegetated and Wet cases document the impact of the drag partition. Finally, the difference between the "Bare and Wet" and Vegetated and Wet cases yields the impact of the herbaceous cover on the dust emission simulations in terms of the fraction of erodible surface, drag partition, and friction velocity.

3. Results

3.1. Soil Moisture and Vegetation

The gravimetric soil moisture at 1 cm depth illustrates the strong variability of the Sahelian rainfall and evaporation during April–September (Figure 1). The first peaks correspond to the first rain events at the beginning of the rainy season in May and June 2008. Until the end of September, soil moisture frequently exhibits high values and strong variations due to rainfall events and the rapid drying of the surface.

During the dry season (October to May), only standing straws or litter are present. The dry herbaceous vegetation decreases progressively and almost totally disappears. Then, a new vegetative cycle begins with germination triggered by the first rains, which occur around June or July depending on the year. Herbaceous growth is very rapid during the summer months, while senescence takes place abruptly in September or October (Figure 2).

The parameters derived from the vegetation measurements (standing mass, fraction of erodible surface, dimensions of the grass patches, roughness density, aspect ratio, and aerodynamic roughness length) reflect this strong seasonality (Figure 3). The end of the dry season (around May and June) is characterized by the presence of the remaining standing straws with mass decreasing from 30 g m^{-2} to a minimum of ~1 g m^{-2}. The maximum standing mass of approximately 150 g m^{-2} coincides with the maximum grass patch dimensions (65 m) reached in late August. Meanwhile, the interpatch mean length increases from ~0.8 m in April to approximately 600 m in June before decreasing during the rainy season to values less than 1 m. Following the

©2014. American Geophysical Union. All Rights Reserved.

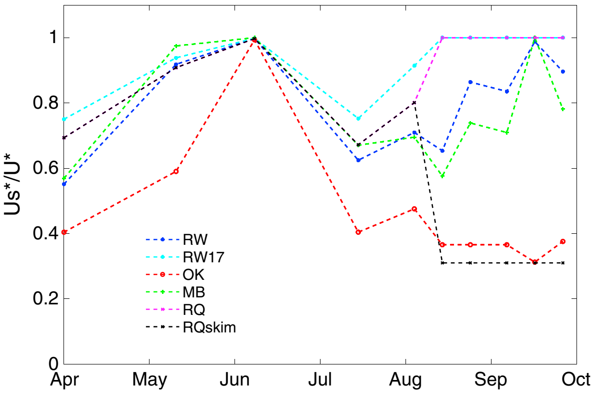

Figure 4. Shear velocity ratios as computed from the various drag partition schemes (RW: Raupach–Walter, RW17: RW with the σ parameter computed from the Agoufou obstacles' dimensions, OK: Okin (integrated value), MB: Marticorena and Bergametti, RQ: Raupach-QUIC, and RQskim: RQ with a skimming flow value), Agoufou site, 2007.

vegetation cycle, the grass height decreases from approximately 0.36 m at the end of the rainy season (October) to 0.05 m at the end of the dry season (June) and increases again during the rainy season. The roughness density (λ, equation (1)) decreases during the late dry season before increasing when vegetation starts growing (from June to August). Then, λ exhibits a decreasing trend in August and September, due to the extension and connection of the grass patches. The λ is on the order of 5.10^{-3} to 5.10^{-2}, which is low compared to, for example, the values up to 0.25 mentioned by *Okin* [2008].

These values of the roughness density are associated with an erodible surface fraction (i.e., the proportion of the surface where vegetation mass is lower than the threshold of 10 g m^{-2}) that can be very low. Because the grass patches are large and flat, they have relatively low frontal area per unit horizontal area and thus low roughness densities despite the large herbaceous cover. The dependence of the roughness density on the geometry of the obstacles is illustrated by the *H*/*W* factor in equation (1). In other words, the study site can be well covered by the herbaceous vegetation, while the roughness density remains low.

The aspect ratios of the grass patches exhibit very high values ($>$100) because of their flat shape, as opposed to the bushes or grass tussocks often reported in the literature. The roughness length (Z_0) has been estimated from the roughness density and the grass height using equation (10). Therefore, Z_0 exhibits a seasonal cycle very similar to that of the roughness density (λ); it reaches its maximum (approximately 1 cm) at the beginning of April and around mid-August, while the minimum values (bounded to z_{0s}) occur either when there is no standing vegetation left, in early June, or when the grass patches are connecting to each other in September.

3.2. Shear Stress Partitioning

Figure 4 represents the evolution over the April–September period of the shear velocity ratio (SVR = u_{S*}/u_*) as simulated by the various drag partition schemes using the input data listed in Table 1 and the vegetation characteristics from Figure 3. The drag partition schemes agree that all the wind energy is exerted on the surface (SVR = 1) at the beginning of June. This is consistent with the absence of nonerodible obstacles at this date. From April until this SVR maximum in June, all the schemes display an increase in the SVR, in agreement with the decrease in roughness density (see Figure 3). From June onward to mid-July, i.e., during the beginning of the rainy season, all the schemes simulate a decreasing SVR due to the vegetation growth. From August to the end of September, the various schemes behave differently: the schemes that depend on λ (i.e., all schemes but OK) exhibit an increasing SVR, except RQskim because of its bounded value for the skimming flow. Additionally, the schemes derived from Raupach's parameterizations (RW17 and RQ) exhibit the same behavior caused by the division by the bare surface ratio (reaching the 1 bounding value), whereas the MB and OK schemes do not present such a limitation. During the period when grass patches are close to each other and cover most of the surface, coming close to a skimming flow regime, OK and RQskim are most likely more realistic than the other schemes.

From a quantitative point of view and as already stated in the literature [e.g., *King et al.*, 2005; *Darmenova et al.*, 2009], the MB and RW schemes are in good agreement, although they have been built on different theoretical bases. In April, the RW17 scheme yields higher SVR values than RW (and MB) because it considers the actual plant geometry through the σ parameter. Indeed, σ varies between approximately 10 to more than 1000 when derived from the field measurements (see Figure 3) used in RW17—while it is equal to 0.125 in RW according to *Walter et al.* [2012]). This parameter is used to apply the available wind energy (i.e., the energy not dissipated on the frontal surfaces of the obstacles) on the surface between obstacles. Thus, for a given

©2014. American Geophysical Union. All Rights Reserved.

roughness density λ, the same energy is applied to a smaller surface for flat obstacles than for thin ones, resulting in a higher SVR.

By definition, the OK scheme yields SVR values ranging from $U_0 = 0.31$, when the interpatch distance D is close to 0, such as around mid-September, to 1, when the obstacles are very distant from each other, such as at the beginning of June. This U_0 value of 0.31 might be considered as a skimming flow value for the SVR, which is greater than 0 because of the herbaceous porosity [*Okin*, 2008]. All the other schemes exhibit generally higher SVR than the OK scheme because of their dependence on λ, which takes rather low values (their SVR would be lower for higher λ). The RQ and RQskim schemes, based on an explicit description of the geometry of herbaceous patches, yield intermediate SVRs that are always bounded by MB and RW. Their behavior is close to the RW and RW17 schemes because they have similar dependency on λ. Their SVR values are similar until August because the grass patches in this period are distant enough not to reach the skimming flow regime.

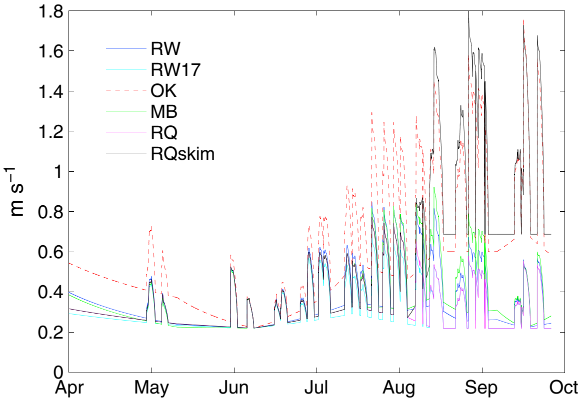

Figure 5. Friction threshold velocities depending on the soil moisture and according to various drag partition schemes (RW: Raupach–Walter, RW17: RW with the σ parameter computed from the Agoufou obstacles' dimensions, OK: Okin (integrated value), MB: Marticorena and Bergametti, RQ: Raupach-QUIC, and RQskim: RQ with a skimming flow value), Agoufou site, 2008.

In summary, at the end of the rainy season, four schemes indicate an increasing SVR: MB because Z_0 depends on λ, RW because it uses functions of λ, RQ which is bounded to one because the fraction of erodible surface becomes very low, and RW17 because the W/H ratio of the obstacles become very high (the grass height remains stable while the grass patch length increases). The OK scheme exhibits a decreasing SVR (integrated over the exposed surface) because of the decreasing interobstacle distance, and the RQskim scheme assumes its lowest value corresponding to the skimming flow regime.

3.3. Threshold Friction Velocities

The threshold wind friction velocity u_t* is a key factor for wind erosion because it controls both the frequency and intensity of the erosion events. Threshold friction velocities are impacted by both changes in soil moisture and variations in vegetation cover (see Figures 1 and 4), as illustrated in Figure 5. This parameter is computed by combining the efficiency of the wind shear stress transferred to the surface computed by the drag partition schemes (i.e., the SVR) and the role played by surface soil moisture (thus, $u_t{*} = u_{tw}{*}/\mathrm{SVR}$, where u_{tw}* is the threshold friction velocity for the wet bare soil obtained from equation (11)). The threshold friction velocity of the dry bare surface is assumed to be $u_{ts}{*} = 0.22\ \mathrm{m\ s^{-1}}$, in agreement with observations on a similar Sahelian sandy soil [*Abdourhamane Touré et al.*, 2011]. However, the spatially integrated representation shown in Figure 5 is not fully adapted for the OK scheme, for which the minimal threshold friction velocity is always u_{ts}* and the friction velocity u* varies spatially in the lee of each obstacle. Thus, the representation of the OK scheme in Figure 5 should be considered a spatially integrated illustration.

As mentioned above, high soil moisture values increase the threshold wind friction velocity u_t*; a decrease in the SVR also produces an increase in u_t*. Thus, the low-frequency variations of the threshold friction velocities are due to the vegetation cover, while their high-frequency variations are due to changes in soil moisture, which is estimated in the same way for all the schemes. Consequently, the differences between these thresholds are due to the differences between the drag partition schemes.

During the end of the dry season, u_t* varies between about 0.60 and 0.30 m s^{-1} for all the drag partition schemes, with a decreasing trend due to the decay of vegetation. During the beginning of the rainy season, u_t* increases from about 0.30 m s^{-1} for all the schemes to approximately 0.80 m s^{-1}. As for the SVR, the largest disagreements between the schemes occur in August and September, when they split into two distinct categories: one with RQskim (and the integrated OK parameterization) leading to u_t* as high as 1.60 m s^{-1} and the other including RW, RW17, MB, and RQ, with u_t* close to 0.40 m s^{-1}. These differences between the drag

©2014. American Geophysical Union. All Rights Reserved.

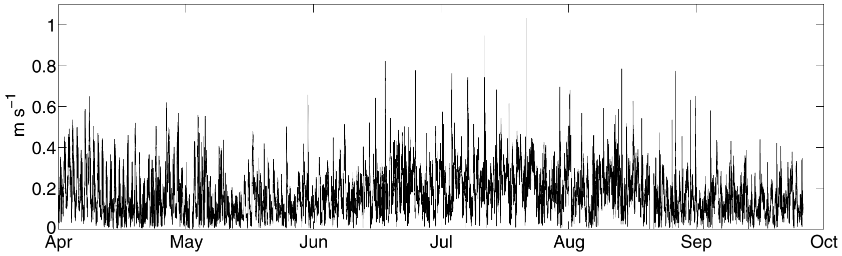

Figure 6. Friction velocity estimated from the wind speed and surface aerodynamic roughness for the vegetated surface case, Agoufou site, 2008.

partition schemes are expected to have a small impact on dust emission because they occur when the fraction of erodible surface is so low (see Figure 3) that dust emissions are expected to be considerably reduced.

3.4. Dust Emissions

The friction velocity is derived from equation (12) for a vegetated surface and from equation (13) for an equivalent bare soil surface for the April–September period, when Z_0 can be estimated from vegetation data. The friction velocity for the vegetated surface (Figure 6) exhibits a seasonal cycle with both higher average values and the highest peaks occurring at the beginning of the rainy season (June and July). The low u_* values are typically lower than 0.20 m s^{-1}, while the peak u_* reach values of 0.60 to 1 m s^{-1}.

3.4.1. Without Vegetation Cover ("Bare" Cases)

For the theoretical Bare and Dry case, the total vertical flux summed over April to September is 574 t km^{-2}, and the frequency of dust emission events (i.e., the proportion of 5 min time steps for which dust emission is simulated) is 15%. For the Bare and Wet case, the total vertical flux summed over the 6 month period is reduced to 417 t km^{-2} and the frequency of dust emission events to 9.9%. This implies that soil moisture induces a limitation of dust emission by 27% in mass.

In terms of the temporal dynamics, the strongest dust emission events occur for both cases at the end of the dry season and the beginning of the rainy season, i.e., from the end of May to the beginning of July (Figure 7). This period corresponds to the fastest wind speeds recorded in the year due to gust fronts caused by convective events [e.g., *Guichard et al.*, 2009; *Abdourhamane Touré et al.*, 2011] (see also Figure 6). The strongest event occurred on 7 July 2008, with 29 t km^{-2} d^{-1} for both cases, with and without soil moisture, because it is a no-rain event. The 10 strongest events (at a daily time scale) represent, respectively, 205 t km^{-2} and 181 t km^{-2} for the "Dry" and "Wet" bare cases and thus 36% and 43% of the corresponding total vertical flux over the 6 month period.

After the beginning of August, dust emissions become very low, mostly because strong winds become weaker and less frequent (see Figure 6). The effect of soil moisture is illustrated in Figure 8: most of it happens during the strong events from June to the beginning of July, when strong winds are associated with rain and thus increases in soil moisture (see Figure 1).

3.4.2. With Vegetation Cover (E Cases and Vegetated Cases)

The effect of soil moisture is also estimated by the differences between the two theoretical cases accounting for the fraction of erodible surface E due to the grass cover (E cases), which reduces the surface from which

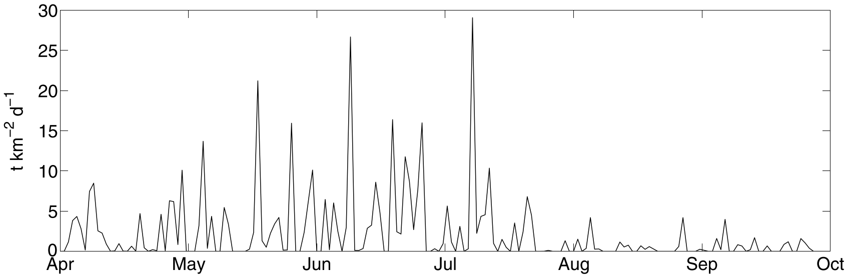

Figure 7. Simulated dust emission from the surface without vegetation, taking into account soil moisture (Bare and Wet case), Agoufou site, 2008.

©2014. American Geophysical Union. All Rights Reserved.

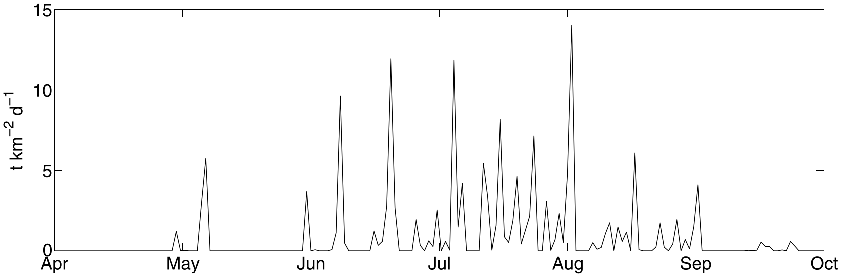

Figure 8. Difference between the Bare and Dry and Bare and Wet cases, illustrating the effect of omitting and including soil moisture without vegetation, Agoufou site, 2008.

dust can be emitted. For the E and Dry case, the dust emission is 686 t km^{-2} for the 6 month period (this is larger than for the Bare and Dry case because of the increase in friction velocity due to the additional roughness induced by the vegetation), while the dust emission for the E and Wet case decreases to 501 t km^{-2} for the 6 month period. Thus, soil moisture induces a reduction in the dust emission of 27%, like in the case of the bare surface.

The effect of the drag partition schemes—which represents the impact of the vegetation on the aerodynamics of the surface layer—is combined with the erodible surface fraction in the "Vegetated" cases. The impact of vegetation is quantitatively illustrated in Table 3 by the difference between the Bare and Wet and Vegetated and Wetcases. In other words, for all the schemes, the impact of the presence of vegetation cover is quantified in terms of mass inhibition, i.e., the difference between the total vertical flux F simulated with (through the fraction of erodible surface, the drag partition, and the friction velocity) and without vegetation cover (neither surface cover nor drag partitioning, bare surface friction velocity), with both cases taking into account the soil moisture.

The total dust emissions over the 6 months of the April–September period, as simulated by using the various dust schemes, vary between 310 and 393 t km^{-2} with an average of 348 t km^{-2} and a standard deviation of 28 t km^{-2}. These values are overall consistent with measurements in Niger by *Rajot* [2001, Table 1], who obtained a maximum horizontal flux of 6000 g cm^{-1} yr^{-1} for a field (200 g cm^{-1} yr^{-1} for a fallow) corresponding to a vertical flux of approximately 60 t km^{-2} yr^{-1} (2 t km^{-2} yr^{-1}) when assuming a ratio of vertical to horizontal flux $\alpha \sim 10^{-6}$ cm^{-1}. Similarly, *Abdourhamane Touré et al.* [2011] observed a mean horizontal flux of 12 kg m^{-1} d^{-1} for a bare plot (3.9 kg m^{-1} d^{-1} for a field covered with crop residues) yielding an estimate of 440 t km^{-2} yr^{-1} for the vertical flux estimate (140 t km^{-2} yr^{-1} with crop residues) using the same α value.

The inhibition of dust emissions due to the grass cover ranges between approximately 6 and 26% (16.5% on average) in mass, depending on the drag partition scheme (Table 3). Similar values are obtained when comparing the Bare and Dry and Vegetated and Dry cases, with the inhibition ranging between 4 and 27% (17.6% on average) in mass (not shown). These results imply that the dispersion between the dust emissions simulated using various drag partition schemes over a herbaceous rangeland is limited. Additionally, they show that the role played by the herbaceous vegetation in limiting dust emissions is similar to the impact of soil moisture on the considered period.

When looking in more detail at the behavior of the different drag partition schemes (Table 3), it can be observed that the RW17 scheme has the smallest inhibition effect due to vegetation cover (393 t km^{-2},

Table 3. Total Simulated Dust Emission, Frequency, and Inhibition (In Mass and % of the Total Flux of the Bare and Wet Case) According to the Different Drag Partition Schemes, Agoufou Site, April to September 2008[a]

Drag Partition Scheme	RW	RW17	OK	MB	RQ	RQskim	Mean	Standard Deviation
Total F (t km^{-2})	310	393	360	333	351	343	348	28
Frequency (%)	10.1	15.0	15.4	10.5	13.2	10.2	12.4	2.5
Inhibition (t km^{-2})	107	24	57	84	66	74	69	28
Inhibition (%)	25.7	5.8	13.7	20.1	15.8	17.7	16.5	7.4

[a] RW: Raupach–Walter, RW17: RW with the σ parameter computed from the Agoufou obstacles' dimensions, OK: Okin, MB: Marticorena and Bergametti, RQ: Raupach-QUIC, and RQskim: RQ with a skimming flow value.

©2014. American Geophysical Union. All Rights Reserved.

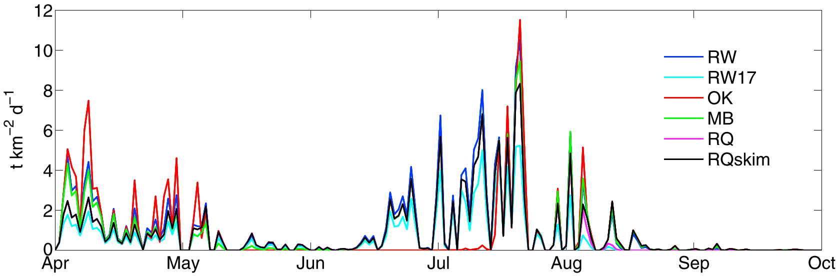

Figure 9. Dust emission inhibition between the E and Wet case and the Vegetated and Wet case for the various drag partition schemes (RW: Raupach–Walter, RW17: RW with the σ parameter computed from the Agoufou obstacles' dimensions, OK: Okin, MB: Marticorena and Bergametti, RQ: Raupach-QUIC, and RQskim: RQ with a skimming flow value), Agoufou site, 2008.

thus ≈ 6% mass inhibition). This low inhibition effect is due to the high aspect ratios of the obstacles, which yield SVR values of 1. Similarly, the relatively strong dust emissions simulated when using the OK scheme were expected because this scheme keeps the friction threshold velocity of the bare surface u_{ts}* between obstacles (which is locally lower than the global increased friction threshold velocity for the other schemes). It must be emphasized that in the present section, the computation of dust emission for the OK scheme uses a spatially varying friction velocity as prescribed by *Okin* [2008], yet with a constant interpatch distance to be consistent with the other schemes (the full model, using an interpatch distribution, may behave differently). The integrated form of this drag partition used above was only presented to provide an integrated illustration comparable to the other schemes (Figures 4 and 5). RQ and RQskim exhibit very similar results, as was expected from the corresponding SVR with a mass inhibition of approximately 16% to 18%. This confirms that the divergence between the drag partition schemes during the late rainy season (in August and September) has little impact on the emission fluxes. The RW scheme leads to the strongest inhibition (310 t km^{-2}, i.e., 25.7% of mass inhibition) because it exhibits the lowest SVR values over most of the 6 month period (see Figure 4). This result is clearly different from RW17, illustrating the sensitivity of the Raupach's scheme to the aspect ratio of the obstacles. The emission fluxes obtained with the RW scheme are similar to the one obtained with MB, confirming the good agreement between *Raupach et al*. [1993] and *Marticorena and Bergametti*'s [1995] schemes. The slight differences in the SVR between these two schemes (mainly during the end of the dry season, thus in May and June) result in nonnegligible differences in the annual dust amounts (respectively, 310 and 333 t km^{-2}).

For all the drag partition schemes, the 10 strongest events occur at the same dates and correspond obviously to the highest wind friction velocities. The strongest dust emission event still occurs on 7 July, with a vertical flux of approximately 30 t km^{-2}, corresponding to approximately 9% of the total vertical fluxes over the 6 month period. The other events take place mostly during June and July, with some occurring at the beginning of May and of August.

The mass inhibition of dust emission due to only the drag partition, i.e., the difference between the theoretical E and Wet case (501 t km^{-2}) and the Vegetated and Wet case (348 t km^{-2} in average), is approximately 30% (31% between the E and Dry and Vegetated and Dry cases, not shown) in mass. This impact is illustrated in Figure 9 in terms of the dynamics. It follows the vegetation cycle, most of it occurring during the end of the dry season (decay of straws) and the beginning of the rainy season (when vegetation starts growing and does not totally prevent erosion yet). The OK scheme exhibits a behavior distinct from the other schemes during June and July because the interpatch distances are very large in this period (see Figure 3); thus, the friction velocity can recover its "undisturbed" value over a large proportion of the surface. Additionally, OK has a strong seasonality because the interpatch length is taken as constant for the sake of comparison with the other schemes (thus enhancing the nonlinear sensitivity to the *x*/*h* factor in equaion (4) by *Okin* [2008]). Using a distribution would smooth this seasonality. All the other schemes exhibit remarkably similar trends.

4. Conclusion

This study assesses the sensitivity of drag partitioning and dust emission simulations to the drag partition scheme in the case of a typical pastoral Sahelian area. Such a site is typically covered with heterogeneous vegetation, mainly composed of herbaceous annuals.

©2014. American Geophysical Union. All Rights Reserved.

The application of the selected drag partition schemes required the characterizing of the grass patches in terms of the width, length, and height, as well as the interobstacle distance. Field measurements were used to determine these dimensions using a random disaggregation method. The size of the grass patches and the interpatch distance show a strong seasonal dynamics driven by the succession of the short rainy season (July to September) and the long dry season (October to June). Grass patches follow these dynamics by growing in length and height and progressively connecting to each other before degrading because of vegetation senescence, herbivory, and trampling.

The shear velocity ratio (SVR) values illustrate the relative behaviors of the drag partition schemes over the Sahelian study site. The comparison of SVR indicates the possible limitations of using the roughness density (λ) to describe the surface of such a site, with large and low grass patches covering much of the surface by the end of the growing season with only litter remaining at the end of the dry season. The comparison also shows the sensitivity of some drag partition schemes to the parameterization of the vegetation cover through its aspect ratio (σ parameter in Raupach's scheme). Erosion studies of areas covered by grass patches, exhibiting a strong seasonal dynamics similar to this Sahelian case, may need to consider these limitations.

Using measured wind speed and soil moisture, a vertical flux of 417 t km^{-2} is obtained for a 6 month period in a theoretical case for which the surface is assumed to be without vegetation. The mass inhibition of dust emission due to the grass cover ranges from 6.4% to 26.8% with respect to the bare soil reference case. The average vertical flux obtained with the different drag partition schemes is 348 t km^{-2} over the 6 month period with a relatively low standard deviation of 28 t km^{-2}. The corresponding mean inhibition due to vegetation is 16.5% in mass with respect to the bare soil situation. Even if these differences are not negligible, they are quite small, suggesting that the different theoretical bases used to build these drag partition schemes have only limited influence on predicting dust emissions when applied to a herbaceous cover, such as those encountered in pastoral Sahelian areas. These results bring new information on dust emission modeling for semiarid areas in terms of vegetation representation and the evaluation of physical models.

Appendix A: Derivation of Vegetation Characteristics From Measurements

At each site and date of observation, each 1 m × 1 m sample plot along the 1000 m long transect is visually classified into four qualitative classes: bare soil and low, medium, and high herbaceous mass. The herbaceous mass of each class is estimated from three to six destructive samples per class (in 1 m × 1 m plots), for which standing (green and dry) vegetation and litter vegetation are separately cut, dried, and weighed.

Disaggregation: The classification is recorded per 10 m × 1 m segment. A disaggregation scheme is used to retrieve mass estimates at 1 m × 1 m resolution. This scheme is based on a two-step randomization: one applied to the qualitative classes and one to the herbaceous mass (Figure A1).

To disaggregate 10 m × 1 m records into the 1 m × 1 m data, a random series of the four classes are determined for each 10 m × 1 m segment along the 1 km line, respecting the number of 1 m × 1 m plots in each class for that given 10 m × 1 m segment. To match three-field observations at the full resolution available for Agoufou (not shown), a significant clumping of classes within a segment is imposed. The result of this *Step 1* is a 1 km line classified at the 1 m × 1 m spatial resolution. *Steps 2 and 3* assign a herbaceous mass value to each 1 m × 1 m plot based on the mean and standard deviation of the herbaceous mass measured for each class, assuming a normal distribution. This produces a series of 1000 mass values along the 1 km line at 1 m × 1 m resolution.

Grass patches are defined as series of consecutive plots above a mass threshold (see below for the threshold derivation). For each date, the average patch length is derived from the 1 km line. The interpatch distance is then estimated assuming that the patches are squares and under the constraint that patch density is consistent with the fraction of erodible surface estimated from the measures (*Step 4*). In other words, the fraction of erodible surface is assumed to be a reliable and important datum, which acts as a strong constraint on the derivation of the patch geometry. When assuming a square shape, the patch length, interpatch length, and total erodible fraction are thus interdependent. We choose to derive the interpatch length from the two other variables. A total of 100 series is obtained for each date; finally, the mean value for each parameter is retained.

Threshold definition: Low herbaceous mass is not always sufficient to protect soil from erosion. A threshold value of herbaceous mass is defined from literature, below which there are risks of soil erosion and above

©2014. American Geophysical Union. All Rights Reserved.

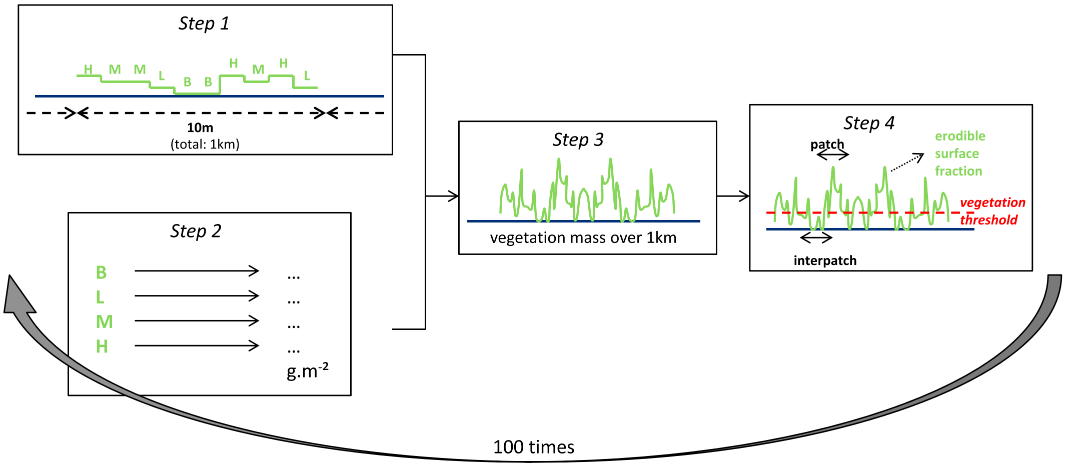

Figure A1. Schematic view of the methodology used to derive the grass patches' dimensions for a given date. "B, L, M, and H" stand for bare surface and low, medium, and high vegetation quantity, respectively.

which the surface is considered to be protected from wind erosion. Previous studies separate the effects of prone and standing vegetation elements on wind erosion. Since *Siddoway et al.* [1965], it is known that "any orientation of residue with respect to the soil surface decreases wind erosion more than the flattened position." Several authors quantified the effect of vegetation on wind erosion using the soil loss ratio (SLR), i.e., the ratio of erosion vertical flux with vegetation divided by the flux from a bare soil [e.g., *Fryrear*, 1985; *Leys*, 1991], but only a few SLR studies address standing vegetation, namely, herbaceous or woody plants. From field measures in four sites covered with salt grass at Owens Lake, *Lancaster and Baas* [1998] indicate that the vertical flux is 10% of the flux measured on bare soil when the vegetation cover is 12%. The vertical flux decreases to 5% when the vegetation cover is 17.5%. This result is confirmed by *Burri et al.* [2011] with wind tunnel experiments using live ryegrass. Accordingly, *Wiggs et al.* [1995] observe that a 14% vegetation cover can be considered a threshold value for wind erosion inhibition in the case of dunes in the Kalahari Desert. Similarly, *Shinoda et al.* [2011] assert that in the case of short grasses, wind erosion is efficiently suppressed by vegetation cover above 15 to 20%. From these experimental works, a standing herbaceous vegetation coverage of approximately 15% appears to reduce wind erosion considerably.

The estimation of the herbaceous mass threshold corresponding to this cover fraction value is based on parameterizations derived from ground measurements [*Mougin et al.*, 1995, equation (26)], which indicate a phytomass of approximately 30 $\mathrm{g\,m^{-2}}$ (in dry matter) for 15% soil cover. In the case of residues lying on the soil, *Abdourhamane Touré et al.* [2011] observed that 10 $\mathrm{g\,m^{-2}}$ of millet crop residues (corresponding to 2% soil cover) is a critical value to limit wind erosion. Thus, a lower bound of 10 $\mathrm{g\,m^{-2}}$ is retained as the limit in the vegetation cover, below which the protective effect against soil erosion is considered to be inefficient, while plots above 10 $\mathrm{g\,m^{-2}}$ are considered to be nonerodible obstacles.

Appendix B: Presentation of the "Raupach-QUIC" Drag Partition Scheme

B1. The QUIC Model

The QUIC model is a semiempirical wind field model; it does not solve the Navier–Stokes equation but is based on empirical parameterizations of the airflow around the obstacles and mass conservation throughout the volume of the domain [*Röckle*, 1990; *Röckle et al.*, 1998; *Kaplan and Dinar*, 1996]. The QUIC model was designed to simulate airflow between buildings and the associated wind fields, in particular to derive pollutant concentrations at fine spatial scale [see, e.g., *Pardyjak and Brown*, 2001, 2002; *Bowker et al.*, 2004].

To reproduce the wind flow and wind erosion in the Chihuahuan Desert (New Mexico, United States), *Bowker et al.* [2006a, 2006b, 2008] developed an approach based on the QUIC model. The surface they considered was strongly heterogeneous with scattered mesquite bushes and large bare soil zones prone to aeolian erosion. Simulations for this well-instrumented site established the capability of the model to reproduce the wind

©2014. American Geophysical Union. All Rights Reserved.

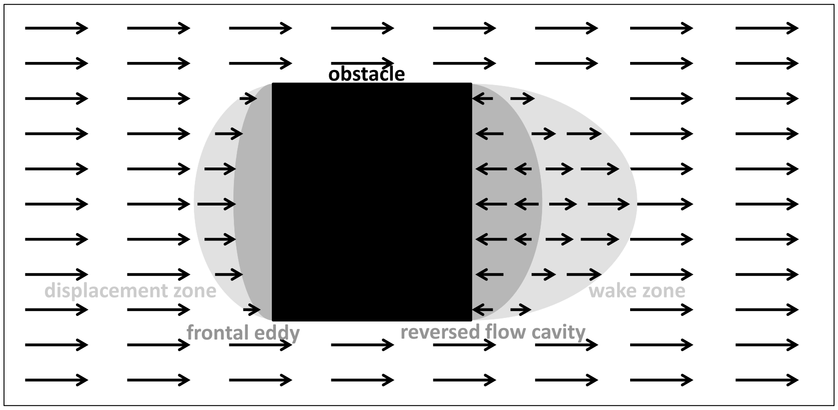

Figure B1. Schematic plan view showing the upwind and downwind cavities of an obstacle in a horizontal plane just above the ground (arrows symbolize the wind speed).

velocity and direction measured at different heights [*Bowker et al.*, 2006a]. When coupled to a dust erosion model, the model also adequately predicts the horizontal fluxes of sediment [*Bowker et al.*, 2006b, 2008].

B2. Parameterizations Derived From the QUIC Model

The size of the zones of perturbed airflows is derived from the QUIC model; the estimate of the shear stress on the bare surface is taken from the literature. For a given obstacle, two main zones of airflow perturbation are defined: one in front of the obstacle and another on its lee side (Figure B1). The airflow perturbation in the lee of the obstacle is in agreement with *Raupach* [1992], who defined the sheltered area and volume downwind of an obstacle where the wind shear stress on the surface is zero. Here the upwind cavity is also taken into account. Because the QUIC model was designed for buildings, the obstacles are parallelepipeds and the perturbed zones are semiellipsoids. The estimation of the length of the perturbed zones on the ground depends on the dimensions of the obstacle (length L, width W, and height H) and on the distance D between two consecutive obstacles [*Bagal et al.*, 2004; *Pardyjak et al.*, 2004; *Singh et al.*, 2006]. The shear stress in the undisturbed area (in white in Figure B1) is called τ_{ext}.

1. *Upwind cavity*

   The original parameterization for the maximum length (perpendicular to wind direction) of the upwind cavity L_f, [*Hosker*, 1984] has been modified in recent studies. *Bagal et al.* [2004] proposed new parameterizations based on wind tunnel measurements of wind speed in the case of rectangular obstacles of various aspect ratios performed by *Snyder and Lawson* [1994]. The new parameterizations distinguish the displacement zone (Figure B1), the length of which is given by

   $$\frac{L_{fx}}{H} = \left(\frac{1.5\frac{W}{H}}{(1+0.8\frac{W}{H})}\right), \tag{B1}$$

   and the frontal eddy, where the wind speed and, thus, shear stress τ are zero [see *Singh et al.*, 2006]:

   $$\frac{L_{fxl}}{H} = \left(\frac{0.6\frac{W}{H}}{(1+0.8\frac{W}{H})}\right). \tag{B2}$$

2. *Downwind cavity*

   The downwind cavity is divided into the reversed flow cavity, where the wind direction is reversed, and the wake zone where the wind flows in the same direction as outside the perturbation but with a lower speed (Figure B1). According to *Röckle* [1990], the length of the reversed flow cavity L_r is given by

   $$\frac{L_r}{H} = \left(\frac{1.8\frac{W}{H}}{(\frac{L}{H})^{0.3}(1+0.24\frac{W}{H})}\right), \tag{B3}$$

   and the length of the wake zone is given by 3 L_r. In the wake zone, the shear stress τ is consequently lower than in the undisturbed area τ_{ext}.

©2014. American Geophysical Union. All Rights Reserved.

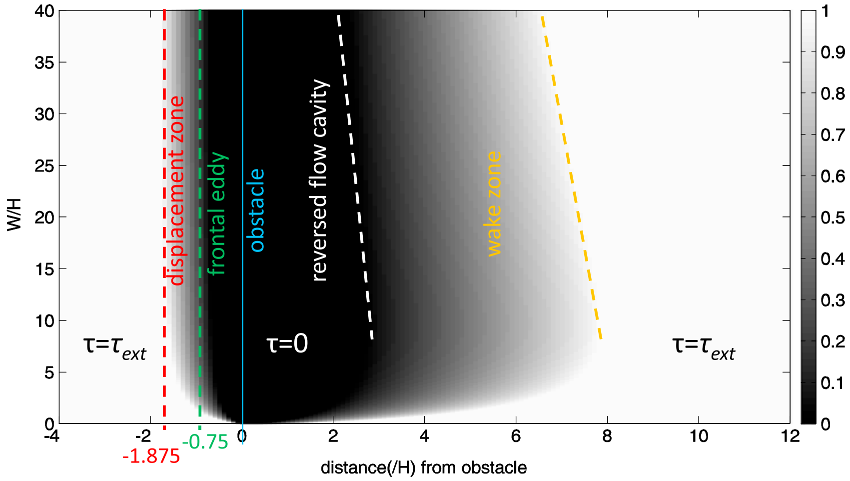

Figure B2. Shear stress ratio τ/τ_{ext} varying with d/H (distance to the obstacle divided by the obstacle height) and the aspect ratio W/H (length of the obstacle divided by its height; here $W = L$).

These parameterizations have been tested by *Pardyjak and Brown* [2001] in the case of an isolated building for several values of the aspect ratio W/H (ranging from 1/4 to 4). The results show a reasonable agreement between the measured and simulated characteristic lengths using equations (B1) to (B3). Strictly speaking, these parameterizations are not fully adapted for porous and flexible vegetation, for which these zones are not as well defined as for a solid obstacle, as illustrated for a vegetated nebkha in the Jornada by *Gillies et al*. [2014]. However, these parameterizations only describe the dimensions of the cavities upwind and downwind of the obstacle. As for the shear stress ratio, the description of its variation in these cavities will be designed as relevantly as possible for a vegetation case (see below).

3. *Interobstacle distances and interferences*

Interference between airflow perturbations occurs if the distance D between the obstacles is smaller than the sum of the wake zone length of a given obstacle and the displacement zone length of the following one. For two identical obstacles, this can be expressed as follows:

$$D < 3L_r + L_{fx}. \qquad \text{(B4)}$$

The dimensions of the perturbation zones upwind and downwind of a given obstacle are used to estimate the shear stress exerted in the different zones for a partly vegetated surface and to assess the shear stress exerted on the surface between obstacles, i.e., on the erodible surface.

B3. Shear Stress on the Erodible Surface

Herbaceous patches are considered nonerodible, and the surface shear stress is only exerted on the bare soil between them. *Arya* [1975] proposed a linear evolution of the shear stress τ between 0 and τ_{ext} in the wake zone downwind of the reversed flow cavity, corresponding to the internal boundary layer. The hypothesis of an increasing shear stress in this area is consistent with *Singh et al*. [2006], *Kaplan and Dinar* [1996], and *Okin* [2008]. A similar behavior of a linearly decreasing shear stress from τ_{ext} to 0 in the displacement zone (excluding the frontal eddy) is assumed. The shear stress in the reversed flow cavity is assumed to be zero, in agreement with the hypothesis of a sheltered area as defined by *Raupach* [1992]; as mentioned above, it is also zero in the frontal eddy.

When the aspect ratio W/H varies from 0 to 40, a distinctive behavior of the shear stress profile is observed for W less than approximately $7H$ (Figure B2). This limit corresponds to a maximum extent of the wake zone relative to the height of the obstacle (i.e., maximum of L_r/H).

For very high W/H aspect ratios (i.e., very "flat" obstacles), the lengths of the displacement zone L_{fx} and of the frontal eddy L_{fxl} tend, respectively, toward $1.875H$ and $0.75H$, whereas the lengths of the reversed flow cavity L_r and of the wake zone ($3L_r$) tend asymptotically toward 0 (see equations (B1) to (B3)).

©2014. American Geophysical Union. All Rights Reserved.

B4. Final Formulation of the Drag Partition

According to *Raupach* [1992, equation (11), p. 382], the area A for which the surface shear stress τ is zero relates to the width (W) and height (H) of an obstacle as follows:

$$\frac{\tau_s(\lambda)}{\tau(\lambda=0)} = e^{-\lambda A/_{WH}}. \tag{B5}$$

The area A, which represents the conceptually equivalent area of the stress deficit due to the obstacle as in *Raupach* [1992], includes the basal area of the obstacle [as in *Raupach*, 1992], of the frontal eddy and of the reversed flow cavity, as well as part of the wake zone and displacement zone basal areas. For the sake of simplicity, these two last contributions are approximated by half the corresponding basal areas. In other words, it is assumed that the shear stress equals $\tau_{\text{ext}}/2$ in the displacement zone and in the wake zone. If A_1, A_2, A_1', and A_2' stand for the basal area of the displacement zone, the wake zone, the frontal eddy, and the reversed flow cavity, respectively, then $A = W^2 + (A_1' + A_2') + 1/2\ (A_1 + A_2)$.

Then, because

$$\frac{\tau_s(\lambda)}{\tau(\lambda)} = \frac{\tau_s(\lambda)}{\tau(\lambda=0)}\ \frac{\tau(\lambda=0)}{\tau(\lambda)} = e^{-\lambda A/_{WH}} \frac{\tau(\lambda=0)}{\tau(\lambda)}\ ,$$

the ratio $\tau(\lambda=0)/\tau(\lambda)$ represents the increase in the total shear stress for a given wind speed at height H above the surface, when the surface roughness increases. This ratio is computed following *Raupach* [1992]: $\frac{\tau(\lambda=0)}{\tau(\lambda)} = \left(\frac{U^*(\lambda=0)}{U^*(\lambda)}\right)^2 = \left(\frac{U^*\ (\lambda=0)}{U_H\ (\lambda=0)}\right)^2 \left(\frac{U_H\ (\lambda)}{U^*\ (\lambda)}\right)^2$, where $U_H(0) = U_H(\lambda)$ because, following *Raupach* [1992], we consider how the stress on the ground varies with λ while U_H is kept constant.

By definition, $\left(\frac{U^*\ (\lambda=0)}{U_H\ (\lambda=0)}\right)^2 = C_S$ (drag coefficient of the bare soil); thus,

$$\frac{\tau_s(\lambda)}{\tau(\lambda)} = e^{-\lambda A/_{WH}}\ C_s\left(\frac{U_H\ (\lambda)}{U^*\ (\lambda)}\right)^2, \tag{B6}$$

where $\left(\frac{U_H\ (\lambda)}{U^*\ (\lambda)}\right)$ can be computed iteratively following *Raupach* [1992].

Finally, the shear stress on the whole surface τ_s is divided by the proportion of bare surface F_{bare} to estimate the shear stress exerted on the intervening surface between the obstacles τ_s':

$$\frac{U_s^*}{U^*} = \sqrt{\frac{\tau_{s'}}{\tau}} = \sqrt{e^{-\lambda A/_{WH}}\ C_s\ \left(\frac{U_H\ (\lambda)}{U^*\ (\lambda)}\right)^2\ \frac{1}{\mathrm{F_{bare}}}} \tag{B7}$$

B5. Skills and Limitations

The drag partition scheme based on Raupach's scheme and QUIC parameterizations has several limitations. The linear change in the shear stress with distance from the obstacle in the displacement zone and in the wake zone is the main assumption of this scheme. Concerning the wake zone, *Arya* [1975] based his hypothesis on *Plate and Lin*'s [1965] measurements behind a single, wedge-shaped model hill. Similarly, *Okin* [2008] proposed an increase in the shear stress in the lee of the obstacle, fitted to *Bradley and Mulhearn*'s [1983] measurements. The case of porous obstacles is not properly dealt with, but the shear stress is assumed to be zero in the reversed cavity (as for Raupach's scheme in the wake zone). This is consistent with *Okin* [2008] assertion that the reversed cavity could be neglected for vegetation because of its porosity.

Despite these limitations, the parameterizations are consistent with previous studies. In the case of Sahelian shrubs, *Leenders et al*. [2011] observed that the wind speed increases progressively until regaining the undisturbed speed at a distance of approximately 7.5H downwind of a shrub of height H. This is in agreement with the length of the wake zone as indicated in Figure 12 for a W/H aspect ratio approximately 5. Similarly, *Okin* [2008] model obtains a shear stress recovery of 90% at 10H downwind of the obstacle, and *Gillies et al*. [2014] reported a 90% recovery at 8H in the case of a nebkha dune (mesquite cover sand mound), which is also consistent with our results.

©2014. American Geophysical Union. All Rights Reserved.

Acknowledgments

We would like to thank the Centre National d'Etudes Spatiales and the research program CAVIARS (ANR-12-SENV-0007-01) from the French Agence Nationale de Recherche for providing financial support to Caroline Pierre during a part of this research work and the AMMA-CATCH observatory (African Monsoon Multidisciplinary Analysis/Couplage de l'Atmosphère Tropical et du Cycle Hydrologique: www.amma-catch.org) for the field measurements. We also thank George Bowker (EPA) for providing useful advice concerning the use of the parameterizations derived from the QUIC model and Jean-Louis Rajot (LISA and IEES) for his relevant advice on wind erosion in Sahelian rangelands. We also thank Manuela Grippa, Nogmana Soumaguel, and Mamadou Diawara (GET) for providing vegetation measurements, pictures, and meteorological data. The data used in this study might be available by request from the authors. Finally, we thank one anonymous reviewer, Gregory Okin, and John Gillies, and the Editor and Associate Editor of the present manuscript for their very helpful comments on the manuscript.

References

Abdourhamane Touré, A., J. L. Rajot, Z. Garba, B. Marticorena, C. Petit, and D. Sebag (2011), Impact of very low crop residues cover on wind erosion in the Sahel, *Catena*, *85*, 205–214, doi:10.1016/j.catena.2011.01.002.

Armas, C., F. I. Pugnaire, and O. E. Sala (2008), Patch structure dynamics and mechanisms of cyclical succession in a Patagonian steppe (Argentina), *J. Arid. Environ.*, *72*, 1552–1561.

Arya, S. P. S. (1975), A drag partition theory for determining the large-scale roughness parameter and wind stress on Arctic pack ice, *J. Geophys. Res.*, *80*, 3447–3454.

Bagal, N. L., E. R. Pardyjak, and M. J. Brown (2004), Improved upwind parameterization for a fast response urban wind model, in *Proceedings of the 84th AMS Conference: Symposium on Planning, Nowcasting, and Forecasting in the Urban Zone*, 45 pp., Seattle, Wash., 7 Jan.

Bagnold, R. A. (1941), *The Physics of Blown Sand and Desert Dunes*, 265 pp., Methuen, New York.

Bergametti, G., and D. A. Gillette (2010), Aeolian sediment fluxes measured over various plant / soil complexes in the Chihuahuan desert, *J. Geophys. Res.*, *115*, F03044, doi:10.1029/2009JF001543.

Boucher, O., et al. (2013), Clouds and aerosols, in *Climate Change 2013: The Physical Science Basis. Contribution of Working Group I to the Fifth Assessment Report of the Intergovernmental Panel on Climate Change*, edited by T. F. Stocker et al. pp. 571–658, Cambridge Univ. Press, Cambridge, U. K., and New York, doi:10.1017/CBO9781107415324.016.

Bowker, G. E., S. G. Perry, and D. K. Heist (2004), A comparison of airflow patterns from the QUIC model and an atmospheric wind tunnel for a two-dimensional building array and a multi-block region near the World Trade Center Site, in *Proceedings of the Fifth Symposium on the Urban Environment/13th Conference on the Applications of Air Pollution Meteorology With the Air and Waste Management Association*, Vancouver, B. C., Canada.

Bowker, G. E., D. A. Gillette, G. Bergametti, and B. Marticorena (2006a), Modeling flow patterns in a small vegetated area in the northern Chihuahuan Desert using QUIC (Quick Urban & Industrial Complex), *Environ. Fluid Mech.*, *6*, 359–384, doi:10.1007/s10652-005-6021-8.

Bowker, G. E., D. A. Gillette, G. Bergametti, B. Marticorena, and D. K. Heist (2006b), Sand flux simulations at a small scale over a heterogeneous mesquite area of the northern Chihuahuan Desert, *J. Appl. Meteorol. Climatol.*, *46*, 1410–1422, doi:10.1175/JAM2537.1.

Bowker, G. E., D. A. Gillette, G. Bergametti, B. Marticorena, and D. K. Heist (2008), Fine-scale simulations of aeolian sediment dispersion in a small area in the northern Chihuahuan Desert, *J. Geophys. Res.*, *113*, F02S11, doi:10.1029/2007JF000748.

Bradley, E. F., and P. J. Mulhearn (1983), Development of velocity and shear-stress distributions in the wake of a porous shelter fence, *J. Wind Eng. Ind. Aerodyn.*, *15*(1–3), 145–156.

Brown, S., W. G. Nickling, and J. A. Gillies (2008), A wind tunnel examination of shear stress partitioning for an assortment of surface roughness distributions, *J. Geophys. Res.*, *113*, F02S06, doi:10.1029/2007JF000790.

Burri, K., C. Gromke, M. Lehning, and F. Graf (2011), Aeolian sediment transport over vegetation canopies: A wind tunnel study with live plants, *Aeolian Res.*, *3*, 205–213.

Chepil, W. S., and N. P. Woodruff (1963), *The Physics of Wind Erosion and its Control*, *Advances in Agronomy*, vol. 15, 302 pp., Academic Press Inc., New York.

Cowie, S. M., P. Knippertz, and J. H. Marsham (2013), Are vegetation-related roughness changes the cause of the recent decrease in dust emission from the Sahel?, *Geophys. Res. Lett.*, *9*, 1868–1872, doi:10.1002/grl.50273.

Crawley, D. M., and W. G. Nickling (2003), Drag partitioning for regularly-arrayed rough surfaces, *Boundary Layer Meteorol.*, *107*, 445–468.

Darmenova, K., I. N. Sokolik, Y. Shao, B. Marticorena, and G. Bergametti (2009), Development of a physically based dust emission module within the Weather Research and Forecasting (WRF) model: Assessment of dust emission parameterizations and input parameters for source regions in Central and East Asia, *J. Geophys. Res.*, *114*, D14201, doi:10.1029/2008JD011236.

De Longueville, F., Y.-C. Hountondji, P. Ozer, B. Marticorena, B. Chatenet, and S. Henry (2013), Saharan dust impacts on air quality: What are the potential health risks in West Africa?, *Hum. Ecol. Risk Assess.*, *19*(6), 1595–1617, doi:10.1080/10807039.2012.716684.

De Rosnay, P., C. Gruhier, F. Timouk, F. Baup, E. Mougin, P. Hiernaux, L. Kergoat, and V. Le Dantec (2009), Multi-scale soil moisture measurements at the Gourma meso-scale site in Mali, *J. Hydrol.*, *375*, 241–252.

Dupont, S., G. Bergametti, and S. Simoëns (2014), Modeling aeolian erosion in presence of vegetation, *J. Geophys. Res. Earth Surf.*, *119*, 168–187, doi:10.1002/2013JF002875.

Fécan, F., B. Marticorena, and G. Bergametti (1999), Parameterization of the increase of the aeolian erosion threshold wind friction velocity due to soil moisture for semiarid areas, *Ann. Geophys.*, *17*, 149–157.

Fryrear, D. W. (1985), Soil cover and wind erosion, *Trans. ASAE*, *28*, 781–784.

Fryrear, D. W., and E. L. Skidmore (1985), Methods for controlling wind erosion, in *Soil Erosion and Crop Productivity*, edited by R. F. Follett and B. A. Stewart, chap. 24, pp. 443–457, ASA-CSSA-SSSA, Madison, Wis.

Gillette, D. A. (1979), Environmental factors affecting dust emission by wind erosion, in *Saharan Dust*, edited by C. Morales, pp. 71–94, John Wiley, New York.

Gillette, D. A., and R. Passi (1988), Modeling dust emission caused by wind erosion, *J. Geophys. Res.*, *93*(D11), 14,233–14,242.

Gillies, J. A., W. G. Nickling, and J. King (2002), Drag coefficient and plant form response to wind speed in three plant species: Burning Bush (*Euonymus alatus*), Colorado Blue Spruce (*Picea pungens* glauca.), and Fountain Grass (*Pennisetum setaceum*), *J. Geophys. Res.*, *107*(D24), 4760, doi:10.1029/2001JD001259.

Gillies, J. A., J. M. Nield, and W. G. Nickling (2014), Wind speed and sediment transport recovery in the lee of a vegetated and denuded nebkha within a nebkha dune field, *Aeolian Res.*, *12*, 135–141, doi:10.1016/j.aeolia.2013.12.005.

Guichard, F., L. Kergoat, E. Mougin, F. Baup, P. Hiernaux, and F. Lavenu (2009), Surface thermodynamics and radiative budget in the Sahelian Gourma: Seasonal and diurnal cycles, *J. Hydrol.*, *375*(1–2), 161–177, doi:10.1016/j.jhydrol.2008.09.007.

Hiernaux, P., E. Mougin, L. Diarra, N. Soumaguel, F. Lavenu, Y. Tracol, and M. Diawara (2009), Sahelian rangeland response to changes in rainfall over two decades in the Gourma region, Mali, *J. Hydrol.*, *375*, 114–127.

Hosker, R. P., Jr. (1984), Flow and diffusion near obstacles, in *Atmospheric Science & Power Production, DOE/TIC-27601*, edited by D. Randerson, chap. 7, pp. 241–326, U.S. Dept. of Energy, Washington, D. C.

Jickells, T. D., et al. (2005), Global iron connections between desert dust, ocean biogeochemistry, and climate, *Science*, *38*(5718), 67–71, doi:10.1126/science.1105959.

Kaplan, H., and N. Dinar (1996), A lagrangian dispersion model for calculating concentration distribution within a built-up domain, *Atmos. Environ.*, *30*, 4197–4207.

Kawamura, R. (1951), Study of sand movement by wind, Univ. Tokyo, Institute for Science and Technology, *Rep.* 5.

King, J., W. C. Nikling, and J. A. Gillies (2005), Representation of vegetation and other non erodible elements in Aeolian shear stress partitioning models for predicting transport threshold, *J. Geophys. Res.*, *110*, F04015, doi:10.1029/2004JF000281.

©2014. American Geophysical Union. All Rights Reserved.

King, J., W. G. Nickling, and J. A. Gillies (2006), Aeolian shear stress ratio measurements within mesquite-dominated landscapes of the Chihuahuan Desert, New Mexico, USA, *Geomorphology*, *82*, 229–244, doi:10.1016/j.geomorph.2006.05.004.

Lancaster, N., and A. Baas (1998), Influence of vegetation cover on sand transport by wind: Field studies at Owens Lake, California, *Earth Surf. Processes Landforms*, *23*, 69–82.

Laurent, B., B. Marticorena, G. Bergametti, and F. Mei (2006), Modeling mineral dust emissions from Chinese and Mongolian deserts, *Global Planet. Change*, *52*, 121–141, doi:10.1016/j.gloplacha.2006.02.012.

Leenders, J. K., G. Sterk, and J. H. Van Boxel (2011), Modeling wind-blown sediment transport around single vegetation elements, *Earth Surf. Processes Landforms*, *36*, 1218–1229.

Leys, J. F. (1991), Towards a better model of the effect of prostrate vegetation cover on wind erosion, *Vegetatio*, *91*, 49–58.

Li, F.-R., L.-F. Kanga, H. Zhanga, L.-Y. Zhaoa, Y. Shiratob, and I. Taniyamab (2005), Changes in intensity of wind erosion at different stages of degradation development in grasslands of Inner Mongolia, China, *J. Arid. Environ.*, *62*, 567–585.

Li, J., G. Okin, J. E. Herrick, J. Belnap, M. E. Miller, K. Vest, and A. E. Draut (2013), Evaluation of a new model of Aeolian transport in the presence of vegetation, *J. Geophys. Res. Earth Surf.*, *118*, 1–19, doi:10.1002/jgrf.20040.

Ludwig, J. A., and D. J. Tongway (1995), Desertification in Australia: An eye to grass roots and landscapes, *Environ. Monit. Assess.*, *37*, 231–237.

Lyles, L., and B. E. Allison (1980), Range Grasses and their small grain equivalents for wind erosion control, *J. Range Manage.*, *33*, 143–146.

MacKinnon, D. J., G. D. Clow, R. K. Tigges, R. L. Reynolds, and P. S. Chavez Jr. (2004), Comparison of aerodynamically and model-derived roughness lengths (zo) over diverse surfaces, central Mojave Desert, California, USA, *Geomorphology*, *63*, 103–113, doi:10.1016/j.geomorph.2004.03.009.

Mahowald, N. M., G. D. Rivera, and C. Luo (2004), Comment on “Relative importance of climate and landuse in determining present and future global soil dust emission” by I. Tegen et al., *Geophys. Res. Lett.*, *31*, L24105, doi:10.1029/2004GL021272.

Marshall, J. K. (1971), Drag measurements in roughness arrays of varying density and distribution, *Agric. Meteorol.*, *8*, 269–292.

Marticorena, B., and G. Bergametti (1995), Modeling the atmospheric dust cycle: 1. Design of a soil derived dust production scheme, *J. Geophys. Res.*, *100*, 16,415–16,430, doi:10.1029/95JD00690.

Marticorena, B., G. Bergametti, D. A. Gillette, and J. Belnap (1997), Factors controlling threshold friction velocity in semiarid and arid areas of the United States, *J. Geophys. Res.*, *102*, 23,277–23,287, doi:10.1029/97JD01303.

Marticorena, B., et al. (2006), Surface and aerodynamic roughness in arid and semi arid areas and their relation to radar backscatter coefficient, *J. Geophys. Res.*, *111*, F03017, doi:10.1029/2006JF000462.

Michels, K. (1994), *Wind Erosion in the Southern Sahelian Zone: Extent, Control, and Effects on Millet Production*, 105 pp., Verlag Ulrich E. Grauer Pub., Stuttgart, Germany.

Minvielle, F., B. Marticorena, D. A. Gillette, R. Lawson, R. Thompson, and G. Bergametti (2003), Relationship between the aerodynamic roughness length and the roughness density in cases of low roughness density, *Environ. Fluid Mech.*, *3*, 249–267, doi:10.1023/A:1022830119554.

Mougin, E., D. Lo Seen, S. Rambal, A. Gaston, and P. Hiernaux (1995), A regional Sahelian grassland model to be coupled with multispectral satellite data. I: Model description and validation, *Remote Sens. Environ.*, *52*, 181–193.

Mougin, E., et al. (2009), The AMMA Gourma observatory site in Mali: Relating climatic variations to changes in vegetation, surface hydrology, fluxes and natural resources, *J. Hydrol.*, *375*(1–2), 14–33, doi:10.1016/j.jhydrol.2009.06.045.

Musick, H. B., S. M. Trujillo, and C. R. Truman (1996), Wind-tunnel modeling of the influence of vegetation structure on saltation threshold, *Earth Surf. Processes Landforms*, *21*, 589–605.

Okin, G. (2005), Dependence of wind erosion and dust emission on surface heterogeneity: Stochastic modeling, *J. Geophys. Res.*, *110*, D11208, doi:10.1029/2004JD005288.

Okin, G. (2008), A new model of wind erosion in the presence of vegetation, *J. Geophys. Res.*, *113*, F02S10, doi:10.1029/2007JF000758.

Okin, G., and D. Gillette (2001), Distribution of vegetation in wind-dominated landscapes: Implications for wind erosion modeling and landscape processes, *J. Geophys. Res.*, *106*(D9), 9673–9683.

Ortiz, A. C., A. Ashton, and H. Nepf (2013), Mean and turbulent velocity fields near rigid and flexible plants and the implications for deposition, *J. Geophys. Res. Earth Surf.*, *118*, 2585–2599, doi:10.1002/2013JF002858.

Ozer, P. (2008), Impact of dust processes on air quality in Niamey, Niger, and consequences on human health, in *Combating Desertification: Assessment, Adaptation and Mitigation Strategies*, edited by D. Gabriels et al., pp. 125–134, UNESCO Chair of Eremology, Bruxelles, Belgium.

Pardyjak, E., and M. Brown (2002), Fast response modeling of a two building urban street canyon, in *Proceedings of the 4th AMS Symposium on the Urban Environment*, pp. LA-UR-02-1217, Am. Meteorol. Soc., Norfolk, Va.

Pardyjak, E., and M. J. Brown (2001), Evaluation of a fast-response urban wind model: Comparison to single building wind-tunnel data, in *Proceedings of the 3rd International Symposium on Environmental Hydraulics*, edited by D. Boyer and R. Rankin, pp. LA-UR-01-4028, 6, Tempe, Ariz.

Pardyjak, E. R., M. J. Brown, and N. L. Bagal (2004), Improved velocity deficit parameterizations for a fast response urban wind model, 84th AMS Conference: Modeling Urban Land Surfaces and Buildings: Part 2. Seattle, Wash. January 7, 45 pp.

Pauley, P. M., N. L. Baker, and E. H. Barker (1996), An observational study of the “Interstate 5” dust storm case, *Bull. Am. Meteorol. Soc.*, *77*, 693–720.

Pierre, C., E. Mougin, B. Marticorena, G. Bergametti, C. Bouet, and C. Schmechtig (2012), Impact of vegetation and soil moisture seasonal dynamics on dust emissions over the Sahelian belt in West Africa, *J. Geophys. Res.*, *117*, D06114, doi:10.1029/2011JD016950.

Pierre, C., G. Bergametti, B. Marticorena, A. Abdourhamane Toure, J.-L. Rajot, and L. Kergoat (2014), Modeling wind erosion flux and its seasonality from a cultivated Sahelian surface: A case study in Niger, *Catena*, doi:10.1016/j.catena.2014.06.006.

Plate, E. J., and C. W. Lin (1965), The velocity field downstream from a two-dimensional model hill, part 2, Rep. CER65EJP14, 63 pp., *Fluid Dynam. Diffus. Lab.*, *Coll. Engin.*, Colo. State Univ., Fort Collins.

Priestley, C. H. B. (1959), *Turbulent Transfer in the Lower Atmosphere*, 130 pp., Univ. Chicago Press, Chicago.

Rajot, J. L. (2001), Wind blown sediment mass budget of Sahelian village land units in Niger, *Bull. Soc. Geol. Fr.*, *172*, 523–531, doi:10.2113/172.5.523.

Raupach, M. R. (1992), Drag and drag partition on rough surfaces, *Boundary Layer Meteorol.*, *60*, 375–395.

Raupach, M. R., D. A. Gillette, and J. F. Leys (1993), The effect of roughness elements on wind erosion threshold, *J. Geophys. Res.*, *98*, 3023–3029, doi:10.1029/92JD01922.

Röckle, R. (1990), Bestimmung der Stomungsverhaltnisse im Bereich komplexer Bebauungsstrukturen, PhD thesis, Vom Fachbereich Mechanik, *der Technischen Hochschule Darmstadt*, Germany.

Röckle, R., C.-J. Richter, T. Salomon, F. Dröscher, and J. Kost (1998), Ausbreitung von Emissionen in komplexer Bebauung - Vergleich zwischen numerischen Modellen und Windkanalmessungen, *Projekt eropäisches Forschungszentrum für Maßnahmen der Luftreinhaltung*, PEF 295002.

©2014. American Geophysical Union. All Rights Reserved.

Rosenfeld, D., Y. Rudich, and R. Lahav (2001), Desert dust suppressing precipitation: A possible desertification feedback loop, *Proc. Natl. Acad. Sci. U.S.A.*, *98*, 5975–5980.

Samain, O., L. Kergoat, P. Hiernaux, F. Guichard, E. Mougin, F. Timouk, and F. Lavenu (2008), Analysis of the in situ and MODIS albedo variability at multiple timescales in the Sahel, *J. Geophys. Res.*, *113*, D14119, doi:10.1029/2007JD009174.

Sassen, K., P. J. DeMott, J. M. Prospero, and M. R. Poellot (2003), Saharan dust storms and indirect aerosol effects on clouds: CRYSTAL-FACE results, *Geophys. Res. Lett.*, *30*, 1633, doi:10.1029/2003GL017371.

Shao, Y., and Y. Yang (2005), A scheme for drag partition over rough surfaces, *Atmos. Environ.*, *39*, 7351–7361, doi:10.1016/j.atmosenv.2005.09.014.

Shao, Y., M. R. Raupach, and J. F. Leys (1996), A model for predicting Aeolians and drift and dust entrainment on scales from paddock to region, *Aust. J. Soil Res.*, *34*, 309–342, doi:10.1071/SR9960309.

Shinoda, M., J. A. Gillies, M. Mikami, and Y. Shao (2011), Temperate grasslands as a dust source: Knowledge, uncertainties, and challenges, *Aeolian Res.*, *3*, 271–293.

Siddoway, F. H., W. S. Chepil, and D. V. Armbrust (1965), Effect of kind, amount, and placement of residue on wind erosion control, *Trans. ASAE*, *8*, 327–331.

Singh, B., E. R. Pardyjak, M. J. Brown, and M. D. Williams (2006), Testing of a far-wake parameterization for a fast response urban wind model, in *Proceedings of the 6th Symposium on the Urban Environment/14th Joint Conference on the Applications of Air Pollution Meteorology With the Air and Waste Management Association Atlanta*, 11 pp., January J8.4A.

Snyder, W. H., and R. E. Lawson (1994), Wind-tunnel measurements of flow fields in the vicinity of buildings, *AMS 8th Joint Conf. on Applic. of Air Poll. Meteor.* with AWMA, Nashville, Tenn., 23-28 Jan.

Swap, R., M. Garstang, and S. Greco (1992), Saharan dust in the Amazon Basin, *Tellus*, *44B*, 133–149.

Tegen, I., and I. Fung (1995), Contribution to the atmospheric mineral load from land surface modification, *J. Geophys. Res.*, *100*(D9), 18,707–18,726, doi:10.1029/95JD02051.

Tegen, I., M. Werner, S. P. Harrison, and K. E. Kohfeld (2004), Relative importance of climate and landuse in determining present and future global soil dust emission, *Geophys. Res. Lett.*, *31*, L05105, doi:10.1029/2003GL019216.

Walter, B., C. Gromke, K. C. Leonard, C. Manes, and M. Lehning (2012), Spatio-temporal surface shear-stress variability in live plant canopies and cube arrays, *Boundary Layer Meteorol.*, *143*, 337–356.

Wang, X., F. Chen, E. Hasi, and J. Li (2008), Desertification in China: An assessment, *Earth Sci. Rev.*, *88*, 188–206.

Webb, N. P., G. S. Okin, and S. Brown (2014), The effect of roughness elements on wind erosion: The importance of surface shear stress distribution, *J. Geophys. Res. Atmos.*, *119*, 6066–6084, doi:10.1002/2014JD021491.

White, B. R. (1979), Soil transport by winds on Mars, *J. Geophys. Res.*, *84*, 4643–4651.

Wiggs, G. F. S., D. S. G. Thomas, J. E. Bullard, and I. Livingstone (1995), Dune mobility and vegetation cover in the southwest Kalahari Desert, *Earth Surf. Processes Landforms*, *20*(6), 515–529.

Wolfe, S. A., and W. G. Nickling (1996), Shear stress portioning in sparsely vegetated desert canopies, *Earth Surf. Processes Landforms*, *21*, 607–619.

Wyatt, V. E., and W. G. Nickling (1997), Drag and shear stress partitioning in sparse desert creosote communities, *Can. J. Earth Sci.*, *34*, 1486–1498.

Yoshioka, M., N. Mahowald, J.-L. Dufresne, and C. Luo (2005), Simulation of absorbing aerosol indices for African dust, *J. Geophys. Res.*, *110*, D18S17, doi:10.1029/2004JD005276.

Youssef, F., S. M. Visser, D. Karssenberg, G. Erpul, W. M. Cornelis, D. Gabriels, and A. Poorting (2012), The effect of vegetation patterns on wind-blown mass transport at the regional scale: A wind tunnel experiment, *Geomorphology*, *159–160*, 178–188.

©2014. American Geophysical Union. All Rights Reserved.